UNIVERSITÀ DEGLI STUDI DI PADOVA

Dipartimento di Fisica e Astronomia “Galileo Galilei”

MASTER DEGREE IN PHYSICS

FINAL DISSERTATION

Analysis of the IFI+Iqueye observations of the Crab pulsar taken around the epoch of the major November 2017 glitch

Thesis supervisor

Prof. Roberto Turolla

Candidate

Stefano Giarratana

Thesis co-supervisor

Dr. Luca Zampieri

Dr. Aleksandr Burtovoi

Academic Year 2019/2020

Abstract

After a catastrophic supernova explosion, the core of a star collapses inwards until the contraction is halted and a new equilibrium configuration is reached. One of the possible stable remnants is the neutron star, where gravity is balanced by nuclear forces and the degenerate pressure provided by neutrons. A peculiar type of neutron star is the pulsar: a highly magnetised, fast rotating compact object which embodies an ideal astrophysical laboratory to study Physics under extreme conditions.

The pulsar emission is characterised by a repeating signal, which usually has a well defined shape and occurs with an accuracy that could compete with that of the atomic clocks. Since this pulsing signal is due to the passage of the beamed emission from the poles of the star across the line of sight of the observer, the rotational period of the neutron star coincides with the time interval between two pulses, which correspond the same pole. Therefore, the analysis of the time of arrival of the pulses is a fundamental tool to constrain the timing behaviour, the rotational evolution and the physical properties of the pulsar. Indeed, albeit the signal coming from a pulsar is remarkably stable, sometimes the neutron star undergoes an unpredictable and sudden spin up event, called glitch, which is usually followed by an exponential decay of the rotational frequency ν towards the pre-glitch values.

In this work we analyzed the time behaviour of the Crab pulsar (PSR B0531+21), which is the young neutron star at the centre of the Crab Nebula, with rotational frequency $\nu \sim 30$ Hz. Until 2017, the Crab pulsar was known to produce glitches with a spin frequency increase of $10^{-9} \leq \Delta\nu/\nu \leq 10^{-7}$; however, around MJD 58064 (8 November 2017), the Crab experienced what is now confirmed to be its largest glitch ever detected: the magnitude of the step increase was $\Delta\nu/\nu = 0.516 \times 10^{-6}$ in the radio band.

We parsed the observations of the Crab pulsar made with the very fast optical photon counter Iqueye, mounted at the 122 cm Galileo Telescope in Asiago through a dedicated optical fiber interface (IFI). The observations were carried out on 2017 October 4 and 7, November 17 and 18, December 30. The timing accuracy and the amount of data available allowed us to pinpoint the major November 2017 glitch in the optical domain and to compare it with the results provided by the Jodrell Bank radio ephemeris. Furthermore, we searched for evidence of changes in the geometry of the emission regions and/or in the magnetosphere of the pulsar possibly induced by the glitch.

Contents

Introduction

Pulsars are highly magnetized, fast rotating neutron stars in which gravity is balanced by nuclear forces and the degeneracy pressure of neutrons. The main characteristic of pulsars is their signal: a repeating pulse occurring with a well defined period, which is due to the passage of the beamed emission across the line of sight of the observer, producing a lighthouse effect [1]. The time interval between two subsequent pulses is therefore interpreted as the rotational period of the pulsar, and by analyzing the variation of the time of arrival of the pulse we can directly study the spin evolution of the pulsar. This high-precision research technique is called Pulsar Timing.

Even if pulsars are generally spinning down due to some braking mechanisms such as the emission of electromagnetic radiation from an accelerated magnetic dipole, the magnetic stresses and the emission of charged particles [2], sometimes they undergo an unpredictable and abrupt increase in the rotational frequency, namely a spin up event with a very short duration, which is called glitch.

One of the most studied neutron stars is the Crab pulsar (PSR B0531+21), which is the young compact object at the centre of the Crab Nebula. It has been monitored regularly in the radio wavelengths since its discovery in 1968 [3] and it is the brightest (V $\sim$ 16.6 mag) neutron star in the optical domain [4]. The Crab pulsar has a rotational frequency $\nu \sim 30$ Hz and a frequency derivative $\dot{\nu} \sim$ -3.77$\times 10^{-10}$ Hz/s [3].

A fundamental characteristic of the Crab pulsar is that it is one of the five isolated neutron stars which show pulsed emission at both optical and radio wavelengths [4]. By parsing the evolution of the phase in different bands we can constrain the geometry of the emission regions surrounding the pulsar. Indeed, the pulsation at a certain wavelength is produced through a given emission mechanism by particles in a given energy range, which can occur only in certain regions of the magnetosphere. [5].

In this work we parsed the observations of the Crab made with the very fast optical photon counter Iqueye [6], mounted at the 122 cm Galileo Telescope in Asiago (Italy) through a dedicated optical fiber interface (IFI) [7]. The observations were performed on 2017 October 4 and 7, November 17 and 18, December 30. We pinpointed the major November 2017 (MJD 58064.555) glitch in the optical domain and we compared it with the results provided by the Jodrell Bank radio ephemeris [8], [9]. We confirmed that the glitch is wavelength independent. Furthermore, we computed the time delay between the radio and the optical phase of the main peak and we found that this time lag dramatically increased after the glitch. If confirmed, this would be the first strong evidence of the time lag variability and a direct evidence of a spatial reconfiguration of the magnetosphere induced by the glitch.

This thesis is structured as follows. In Chapter 1 we introduce the fundamental Physics concerning neutron stars, the timing techniques and the Crab Nebula pulsar. After a brief presentation of the glitch phenomenon and the instrumentation used (IFI+Iqueye), we show the data reduction and analysis in Chapter 2. In Chapter 3 we present the main results, which are further discussed in Chapter 4.

Chapter 1

Scientific Framework

The fate of a star is determined by the struggle between gravity, which tends to compress the mass inwards, and outwards forces such as gas pressure and radiation pressure given by nuclear reactions. When massive stars run out the fuel, nuclear reactions are depleted and the inwards action of gravity is no longer balanced: while the outer layers of the star are violently ejected in a catastrophic outburst called supernova explosion, the core of the star collapses until it reaches a new equilibrium. The stable remnant left behind is a neutron star, where gravity is balanced by nuclear forces and the degeneracy pressure of neutrons. Indeed, as the mass density ρ increases ($\rho \sim 10^3$ g/cm^3) under the action of gravity, the electrons cannot be described with an ideal gas law, and quantum mechanics is needed: according to the Heisenberg's uncertainty principle ($\Delta p \Delta x \approx \hbar$) and the Pauli's exclusion principle for fermions, the electrons must posses large momenta and cannot occupy the same quantum state. These large quantum mechanical momenta provide the so called degenerate pressure. As ρ further increases, the degenerate electrons become relativistic and, when their total energy exceeds the mass difference between the neutron and the proton, $E=\gamma m_e c^2 \geq (m_n - m_p) c^2 = 1.29$ MeV, the inverse β decay process $p + e \rightarrow n + \nu + e$ can convert protons into neutrons, with the emission of a neutrino ν. Albeit in an ideal gas neutrons would decay into protons and electrons with a mean lifetime of 14.8 minutes, in a degenerate gas this cannot occur because there are no available quantum states for the ejected electron to occupy [10]. Finally, when $\rho \sim 10^{14}$ g/cm^3, the neutrons become degenerate, contributing the required pressure to sustain the gravity in the case of neutron stars.

A particular type of neutron star is a pulsar: a fast rotating neutron stars with a very large magnetic field, $B \simeq 10^{12}$G. The main feature of pulsars is the signal we detect: a repeating pulse occurring with a well defined period, which is interpreted as the rotation period of the neutron star. Hitherto the distribution of the pulse periods among pulsars is bimodal [11]: one group is found in a period range of 0.1-10 seconds, while the other is found at 1-10 milliseconds.

Thanks to their peculiar properties, pulsars represent a powerful and complete laboratory to study physics under extreme conditions which cannot be reached on Earth. Indeed, studying these objects can shed light on the behaviour of a plasma embedded in a very high magnetic field, on the nuclear interaction between neutrons, on the degenerate pressure which sustains gravity, on the theory of General Relativity [12] and on the dynamics of a neutron superfluid [13]. Thus, they offer a special environment where Electromagnetism, Theoretical Physics, General Relativity, Nuclear Physics, Fluid Dynamics and Physics of Matter mix together. A satisfactory understanding of neutron stars requires a deep knowledge of these disciplines.

The first crucial property for the detection and the investigation of pulsars is their periodic signal: in this thesis we exploit the pulsar timing, i.e. the analysis of the arrival times of the pulses, of the Crab pulsar (PSR B0531+21) to probe the structure and evolution of the magnetic field and the geometry of the emission regions.

In the following sections we give a brief overview of the fundamental physics concerning neutron stars and of the timing techniques needed to analyze their behaviour. Finally we focus on the Crab pulsar. We refer to [2] for further information.

1.1 Neutron Stars

1.1.1 Introduction

After the discovery of the neutron in the 1930's by Chadwick, the idea of a stellar object made up of neutrons formed in the aftermath of a supernova explosion was first proposed by Baade and Zwicky in 1934 [14]. The interest further increased after the detection of discrete X-ray sources by Giacconi in 1962 [15]. Indeed, up to then the solar-like stars were considered the dominant population of X-ray emitters but too weak to be detected. Thus, the need of a new class of objects became clear soon. The turning point came with the discovery by Bell and Hewish in 1967 of a repeating signal in the radio band with a well-defined shape [16]. This turned out to be the first detection of a pulsating radio source. After this, many other objects were discovered with similar properties and they were called Pulsars. To identify a source of this type we use the nomenclature PSR followed by its right ascension and the declination. So, for example, the Crab Nebula Pulsar is PSR B0531+21.

The pulses were first explained as oscillations of compact stars until Gold 1968 [1] suggested what is now universally accepted as the most realistic physical model: a rotating neutron star with beamed emission producing a lighthouse effect. Before going into the details of this object, we expose the historical argument which led to Gold's explanation [2]. Let's consider first the observational evidence, namely (i) the magnitude of the periods, ranging from milliseconds to several seconds, (ii) the stability of the average pulses, (iii) the overall increase of the rotational periods with times. We consider some possible models, such as oscillations of compact objects, binary systems, rotating white dwarfs, satellites orbiting a neutron star.

If we consider a rotating object with mass M and radius R, the maximum angular velocity Ω is determined by equating the centrifugal and the gravitational forces:

$$\Omega^2 R \simeq \frac{GM}{R^2} \tag{1.1}$$

where G is the gravitational constant. Since $M/R^3 \sim \rho$, where ρ is the mass density, eq.(1.1) can be written as $\Omega \simeq (G\rho)^{1/2}$. Taking $P = 2\pi/\Omega$ as the rotation period, we can exploit this timescale to exclude the rotating white dwarf model and the oscillations of white dwarfs and neutron stars. Indeed, the fundamental oscillations modes are of the same order of magnitude of the breakup period [2]: white dwarfs have $\rho \sim 10^7$-10^8 g/cm^3, thus their fundamental modes lie in the $2-10$ s range, while neutron stars have $\rho \sim 10^{14}$ g/cm^3 and their fundamental modes are in the 1-10 ms range. A rotating white dwarf can have a minimum period (corresponding to the maximum angular velocity given by eq.(1.1)) of the order of seconds, thus it cannot explain the millisecond pulsars. Concerning the binary systems, we can imagine two situations: (1) two compact objects orbiting around each other or (2) a satellite orbiting a star. Once again, to get a timescale we equate the gravitational attraction and the centrifugal force, recovering in the first case eq.(1.1) with M replaced by the total mass, let's say $2M$ for two stars with the same mass, and the orbital radius R replaced by $2R$. We would get again $\Omega \simeq (G\rho)^{1/2}$ and a timescale consistent only with a neutron star binary. However, by emission of gravitational waves the system would be unstable, spiraling and finally merging. For the second case, to get a reasonable timescale we should have a low mass object orbiting the star, which would be torn apart by the huge gradient in the gravitational field of the compact object [2]. Finally, considering the rotation of a neutron star we get from eq.(1.1) a minimum period of the order of ms, which is consistent with observations. Thus, pulsars are rotating neutron stars.

The next step is to explain the observed deceleration and the physical mechanism which produces the observed emission. To answer to the first question, let's consider a rotating object with moment of inertia I and angular velocity Ω. Its rotational energy is:

$$E_{rot} = \frac{1}{2} I \Omega^2 \tag{1.2}$$

and thus the time derivative is:

$$\dot{E}_{rot} = I\Omega\dot{\Omega} + \frac{1}{2}\dot{I}\Omega^2 \approx I\Omega\dot{\Omega} \approx -4 \times 10^{32} I_{45} P^{-3}(s) \dot{P}_{-14} \text{ erg s}^{-1} \tag{1.3}$$

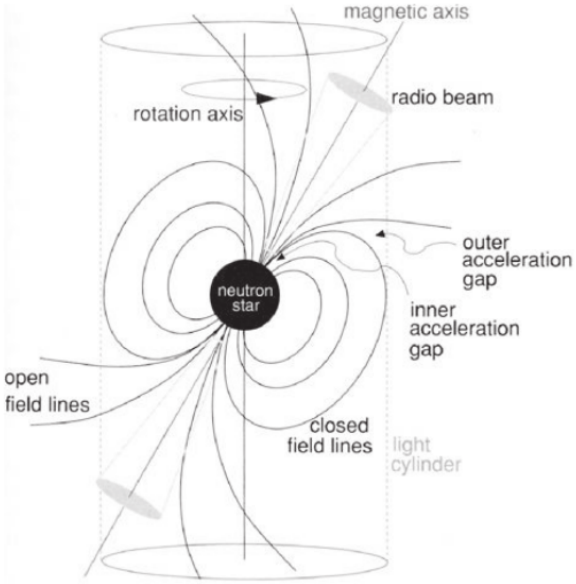

Figure 1.1: Schematic representation of a pulsar as a magnetized neutron star with misaligned rotation and magnetic axes. The radio pulses are associated with the passage of the radio beams across the line of sight to the observer. Figure taken from [10].

where we consider the changes in the moment of inertia negligible, and I_{45} is the moment of inertia in units of 10^{45} g cm^2. Using this simple expression we can infer the energy loss from the measurements of the period and the time derivative of the period. The pulsars' magnetic field can be considered, as a first order approximation, as a dipole magnetic field, with the dipole moment μ forming an angle α with the rotation axis (otherwise we would not see pulsations). The energy loss of an accelerated dipole moment is [2]:

$$\dot{E}_{rot} = \frac{2\mu^2\Omega^4 \sin^2\alpha}{3c^3} \approx 10^{31} B_{12}^2 R_6^6 P^{-4}(s) \sin^2\alpha \text{ erg s}^{-1} \tag{1.4}$$

where B_{12} is the magnetic field in units of 10^{12}G and R_6 is the stellar radius in units of 10^6 cm. Equating the expressions (1.3) and (1.4) we get the magnetic field:

$$B_{12} \approx \frac{6\sqrt{I_{45}\dot{P}_{-14}P(s)}}{R_6^3 \sin\alpha} \tag{1.5}$$

However, this is not the radiation we measure from the pulses: the corresponding signal has frequency $\nu = \Omega/2\pi \sim$1-10 Hz and sinusoidal shape, while the pulsations we detect lie in radio frequency $\nu \sim$10 MHz - 10 GHz and show narrow peaks covering a small fraction of the rotation period. Indeed, the rotational energy we computed is used mainly to accelerate charged particles to high energies, which interact afterwards with the surrounding nebula (in the case of young pulsars like the Crab Nebula pulsar), leading to a strong emission in the electromagnetic spectrum. We further discuss the emission mechanisms in section 1.1.4.

Therefore, we end up with a simple model (Figure 1.1): a magnetized neutron star with the magnetic and rotation axes misaligned; the pulse we detect is assumed to be due to the passage of the radio beams from the poles across the line of sight of the observer; the spin-down is caused by some braking mechanisms such as the emission from an accelerated magnetic dipole.

1.1.2 Structure of Pulsars

In the previous section we introduced a simple description for a magnetized neutron star, in order to provide a general picture of the physical environment we are dealing with. The next step is the refinement of the model to get information about the structure: first of all, since pulsars are compact

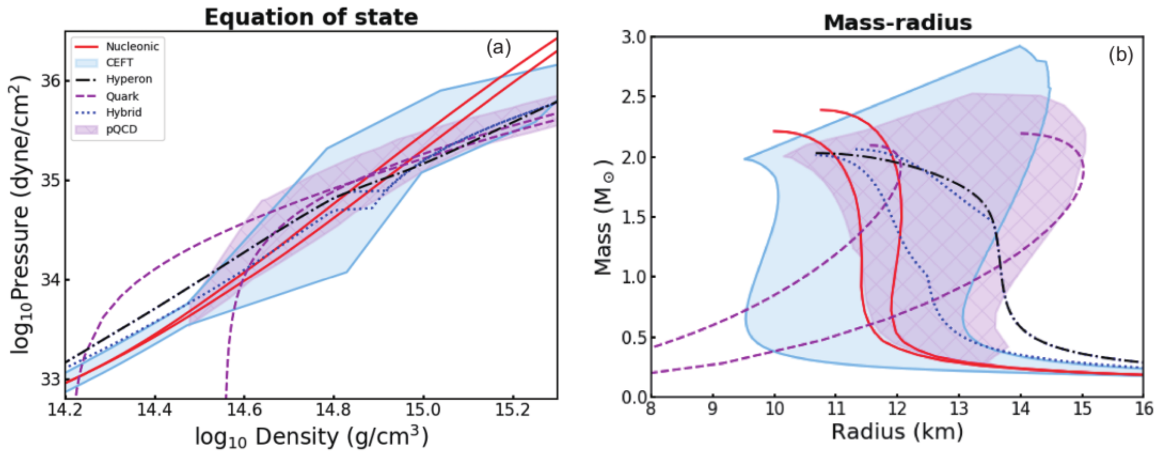

Figure 1.2: The pressure-density relation (EoS) (a) and the mass-radius relation (b) for different models as discussed by [17]: Nucleonic (models AP3 and AP4); Quark (u, d, s quarks); Hybrid (inner core of u, d, s quarks, outer core of nucleonic matter); Hyperon (inner core of hyperons, outer core of nucleonic matter). The range of nucleonic EOS based on Chiral Effective Field Theory is indicated as CEFT. Figure taken from [17].

objects with a strong gravity gradient, we need a general theory for gravitation. In this work we assume the General Relativity (GR) theory as the correct prescription. Within this framework, the solution for masses, radii and the overall structure of spherically symmetric objects in hydrostatic equilibrium are given by the Tolman-Oppenheimer-Volkoff (TOV) equation:

$$\frac{dP(r)}{dr} = -\rho(r)\frac{Gm(r)}{r^2}\frac{[1+\frac{P(r)}{\rho(r)c^2}][1+\frac{4\pi r^3 P(r)}{m(r)c^2}]}{1-\frac{2Gm(r)}{rc^2}} \tag{1.6}$$

where r is the radial distance, starting from the center of the object and going outwards, $P(r)$ is the total pressure at radius r, ρ(r) is the density at radius r, G is the gravitational constant, $m(r)$ is the mass inside the sphere with radius r and c is the speed of light. The solution is usually calculated by integrating eq.(1.6) numerically, once the Equation of State (EoS) is given. The EoS is the fundamental relation which links the pressure and the density of matter inside the neutron star. An EoS is called *stiff* if the pressure depends strongly on density, so that a small change in density will cause a large change in pressure; conversely, an EoS is called *soft* whenever the pressure is not changing significantly with density (Figure 1.2(a)). Therefore, the choice of the EoS can considerably affect the solution. The derivation of the EoS is an active and complex research field, which is beyond the purpose of this thesis, so we just show some EoS used for the neutron star structure in Figure 1.2(a) taken from [17] and we refer to [18] for a detailed review on this topic. To provide a quantitative grasp of the solutions for different EoS, we focus on the mass-radius relation (Figure 1.2(b)). We can consider a very soft and a very stiff EoS: a Nucleonic EoS, which considers only neutrons and protons (models AP3 and AP4 [17]) and a Hyperon EoS, which consists of an inner core of hyperons and a outer core of nucleonic matter [17]. Indeed, the presence of non nucleonic phases, namely hyperons or condensates, reduces the pressure and therefore "softens" the EoS [18]. The first crucial characteristic of many of these curves is that the radius is almost independent from the mass: even if the radius R decreases with increasing mass M in all the cases, stiffer EoS generally provide a roughly constant radius over most of the mass range, and the radius rapidly decreases with increasing mass only in the smallest masses limit M $<$ 0.4 M$_\odot$. By contrast, softer EoS provide a smoother decrease of the radius with increasing mass and they usually lead to smaller maximum masses. Another important characteristic is that the mass-radius relations predict a maximum mass beyond which there are no stable solutions [18].

Concerning the internal structure of the neutron star, the accepted model consists, from the surface inwards, of [2]:

- Solid outer crust (from $\rho \approx 10$ g/cm^3 to $\rho_{drip} \approx 4\times10^{11}$ g/cm^3): up to $\rho \approx 8\times10^6$ g/cm^3 it's a

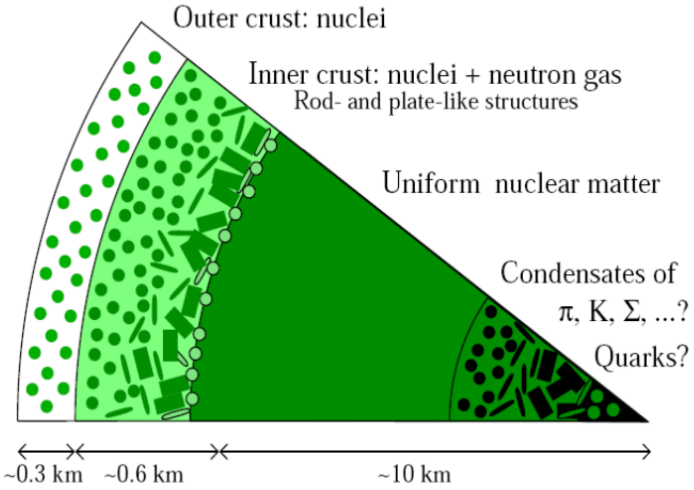

Figure 1.3: Schematic view of the interior structure of a 1.4 $M_\odot$ neutron star. Figure taken from [2].

coulomb lattice of Fe nuclei surrounded by a sea of electrons. For $8\times10^6 \leq \rho \leq 4\times10^{11}$ g/cm^3 the crust is still a Coulomb lattice of nuclei in an electron sea, but the nuclei are progressively neutron-richer as density increases.

- Solid inner crust (from $\rho_{drip} \approx 4\times10^{11}$ g/cm^3 to $\rho_{nm} \approx 2.8\times10^{14}$ g/cm^3): it is a lattice of nuclei surrounded by neutrons and the whole assembly is immersed in an electron sea. In this range there could exist non-spherical nuclei, i.e. rods and plates. Typical thickness of the outer crust is 0.3 km, while the inner is 0.7 km, for a total of 10% of the neutron star radius. The mass contained in the crust is 0.012 $M_\odot$, i.e. $\sim$1% of the total mass.

- Liquid outer core (from ρ_{nm} to $2\rho_{nm}$): uniform nuclear matter made of neutrons with a small amount of protons and electrons (due to β-stability).

- Liquid inner core (from $2\rho_{nm}$ to $\rho_c \approx$ 4-7ρ_{nm}): this range is still highly debated. We do not know exactly what is happening in the inner core, but there are some suggestions involving hyperions, which are very likely to appear for $\rho \geq$ 2-3ρ_{nm}, or a meson condensate (π^-, π^0, K^-). Indeed, π^- may occur at $\rho \geq 1.5\rho_{nm}$, π^0 may occur at $\rho \sim$ 1.5-2ρ_{nm} and K^- may occur at $\sim 5\rho_{nm}$.

Furthermore, quark matter can appear for $\rho \geq$ 2-6ρ_{nm}. The appearance of exotic forms of matter soften the EoS. But, as for example for the meson condensate, they may operate in a so small density range that they do not affect the overall properties. A schematic view of the interior of a neutron star is shown in Figure 1.3, taken from [2].

1.1.3 Magnetosphere

A complete model for pulsars needs a satisfactory description of the environment surrounding the neutron star, i.e. the magnetic topology, of the dynamics which rules the particles acceleration and of the radiative mechanisms. Calling magnetosphere the region where the physics is dominated by the overwhelming magnetic field of the star, the electrodynamics occurring in the magnetosphere is a complex task to undertake, thus simpler models were developed hitherto. The detailed calculations are beyond the aim of this thesis, then we just provide a summary here. We refer to [10], [2] and [19] for detailed explanations.

The first model was proposed by Pacini in 1967 [20]. Let's consider a vacuum magnetosphere, depleted of any plasma or particle. First of all, we shall consider the neutron star as a superfluid with an electric conductivity so high that the magnetic field is frozen into the star, and can last for a long time [21]. If the magnetic dipole moment p_o is aligned with the rotation axis, the electric field in the corotating frame vanishes [21], i.e. E'=0. We emphasize that the transformation from an inertial to a rotating frame must be done in General Relativity, and does not reduce to the Lorentz transformations.

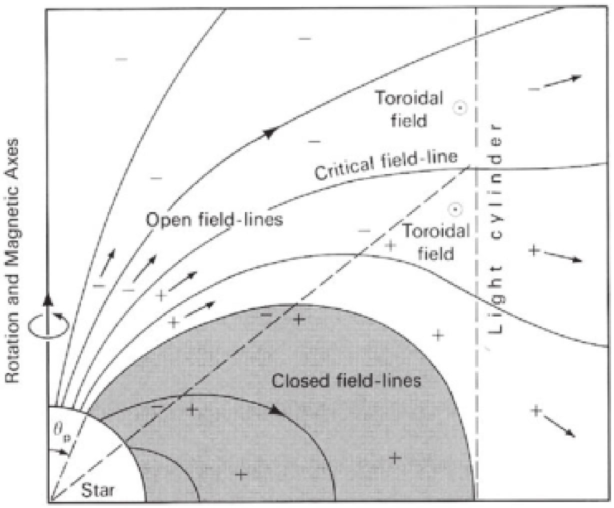

Figure 1.4: Schematic view of magnetosphere proposed by Goldreich and Julian. The neutron star is at the lower left. The toroidal component of the open field lines is perpendicular to the picture. Flowing charges are represented by a plus or minus sign. Figure taken from [10].

Thus, from the General Relativity transformations of the electric field and the Maxwell equation we obtain:

$$E' = E + \frac{(\Omega \times r)}{c} \times B = 0 \tag{1.7}$$

where r is the position vector, Ω is the angular velocity of the neutron star, E is the electric field in the inertial frame and c is the speed of light. From eq.(1.7) we get that the magnetic and the electric field are perpendicular, thus $E \cdot B$=0. From Gauss' law $\nabla \cdot E = \rho_e/\epsilon_o$, with ρ_e the internal charge density and ϵ_o the dielectric constant, a charge distribution within the star is found, and it must match the external vacuum solution given by the Laplace's equation $\nabla^2 E = 0$. The external electrostatic potential will be quadrupolar:

$$\phi_{out} = \frac{-B_o\Omega}{3c}\left(\frac{R}{r}\right)^5 r^2 P_2(\cos\theta) = \frac{-B_o\Omega}{6c}\frac{R^5}{r^3}(3\cos^2\theta - 1) \tag{1.8}$$

where B_o is the magnetic field at the pole, R the radius of the sphere, P_2 the Legendre polynomial of the second order. Using eq.(1.8) and Gauss' law, a charge density is found at the surface of the neutron star as well. In 1969 Goldreich and Julian [22] realized that the vacuum approximation would not be stable in this case, because differentiating eq.(1.8) in the radial direction an induced electric field is obtained at the surface, $E_{\|} \approx 10^{13}$ V/m. This electric field overcomes the gravitational bond and the Coulomb lattice interaction [19], extracting charges from the stellar surface. Indeed, taking the ratio between the Coulomb force and the gravitation attraction for a proton one gets [19]:

$$\frac{f_{em}}{f_{grav}} = \frac{eE_{\|}R^2}{GMm_p} \approx 10^9 \tag{1.9}$$

and a value 2000 larger for electrons. Thus a fully conducting plasma is injected in the magnetosphere surrounding the neutron star, and charged particles can flow along the magnetic field lines. Even if it turns out to be unstable, the vacuum model can be appropriate for low-density plasmas, i.e. n $<$ 19 particles/m^3, as that inferred for the Crab Pulsar [19].

If the plasma is bound to the field lines, then it will corotate with the star at the angular velocity Ω, provided that the magnetic field has no toroidal component. At a certain distance the velocity of the plasma would exceed the speed of light, which is forbidden from Special Relativity: therefore, there is an upper limit to the distance from the neutron star for which the plasma can corotate with the pulsar, $R_l = c/\Omega \approx 10^9$ cm. This bound is called the light cylinder. This fact is valid also for the magnetic field lines: those crossing the light cylinder must be open and acquire a toroidal component. The closed lines which do not cross the cylinder form the magnetosphere. Through the open field lines, charges can flow outwards, becoming highly relativistic and reaching regions very far from the star (see Figure 1.4). The open lines will be bent backward with respect to the stellar rotation, inducing magnetic stresses on the neutron star which oppose to the rotation. An estimate of the order of magnitude for this effect is given by $\mathrm{B}_p\mathrm{B}_\phi/4\pi$ where B_p and B_ϕ are the poloidal and the toroidal components of the magnetic field respectively. By integrating the stresses over the light-cylinder surface a magnetic torque is obtained [2]:

$$N = -\frac{K\mu^2\Omega^3}{6c^3} \tag{1.10}$$

where $K \sim 1$ is a constant depending on the detailed structure of the magnetic field, μ is the magnetic dipole moment. The torque will extract energy with a rate

$$\dot{E}_{rot} = N\Omega = -K\frac{\mu^2\Omega^4}{6c^3} \tag{1.11}$$

This expression turns out to be of the same order of magnitude of eq.(1.4) with $\sin\alpha \sim 1$, which was found for the electromagnetic emission from a magnetic dipole whose rotation and magnetic axes are not aligned, i.e. the oblique rotator. Thus, both configurations (aligned and oblique rotators) lead to the same kind of braking torques. Therefore, for a general oblique rotator we expect both of them to act on the spin-down evolution of the neutron star.

We conclude this section providing a recap on the basic features of the magnetosphere, as summarized in [19]:

- a light cylinder, where the rigid body velocity of a corotating particle or field line reaches the speed of light.
- a plasma which is corotating with the neutron star up to the light cylinder R_l, screening the electric field such as $E \cdot B = 0$. Thus, no acceleration along field lines is permitted. However, deviations from this condition lead to electromagnetic activity.
- a magnetic topology with both closed and open lines: the former are well within the light cylinder and have no toroidal component. The latter cross it and are bent "backwards" with respect to the rotation of the neutron star. Particles on these field lines can escape freely to infinity.
- polar caps, i.e. regions on the stellar surface located around the magnetic poles, where open field lines are anchored. The radio emission is supposed to be generated here.
- a light surface, where the intensity of the electric field equals that of the magnetic field. Here particles suffer an acceleration. The light surface and the light cylinder do not coincide, and the former can be at infinity for sufficiently strong longitudinal currents. The theory of MagnetoHydroDynamics cannot be applied here.
- slot gaps: small volumes along the last closed field line, empty of charges. Pair creation is allowed, and emergence of high energy radiation and acceleration of particles are supposed to take place.
- outer gaps: almost empty volumes in the magnetosphere, between the null surface, i.e. where ρ=0, and the last closed field line. Electron-positron pair creation and synchrotron emission are generated also here.

1.1.4 Emission Mechanisms

Albeit the magnetic dipole emission (eq.(1.4)) and the magnetic braking (eq.(1.11)) can explain the pulsar spin-down, the observed pulsing emission must be generated through some specific radiating mechanisms. The first step we face is the characterisation of the emission: is it coherent or non-coherent? We define an emission as coherent whenever there is a defined phase relation between the emitting components of the source. First, let us consider the surface brightness of a isotropic source $I(\nu)$ at a given frequency ν, so that the energy emitted per second per unit surface area per unit solid angle:

$$I(\nu) = \frac{c\epsilon(\nu)}{2\pi} \tag{1.12}$$

where $\epsilon(\nu)$ is the energy density and c is the light speed. Let us consider the radio emission: to estimate $\epsilon(\nu)$ we assume that the source is in local thermodynamic equilibrium and approximate $\epsilon(\nu)$ taking the Rayleigh-Jeans limit ($h\nu \ll kT$):

$$\epsilon(\nu) = \frac{8\pi kT\nu^2}{c^3} \tag{1.13}$$

where k is the Boltzmann constant and T is the brightness temperature, i.e. the temperature a blackbody would have if its surface brightness were the observed one. Inserting eq.(1.13) into eq.(1.12) and solving for T:

$$T(\nu) = \frac{I(\nu)c^2}{4k\nu^2} \tag{1.14}$$

For the radio emission of pulsars, the brightness temperature would be $T \sim 10^{25}$ -10^{31} K, which is too high to be explained by a non-coherent emission process.

The next step is to identify which types of physical mechanisms could lead to a coherent emission. Concerning the radio emission, according to [23] there are five possible mechanisms occurring: (i) the maser curvature emission, (ii) the relativistic plasma emission, (iii) linear acceleration emission, (iv) anomalous Doppler instability and (v) curvature-drift instability. We restrict ourselves to the discussion of the first two mechanisms, referring to [23] and [2] for a detailed analysis.

Maser emission occurs when waves are amplified due to negative absorption in a medium which has a so-called inverted population, so that the particle density at higher energy levels is higher than that at lower energy levels.

Among the relativistic plasma emission processes, the best known involves a beam-plasma instability. It involves three main steps: first, a beam of particles passing through a plasma generates an instability; second, this instability results into a turbulent motion inside the plasma; finally, the turbulent energy is converted in radiation through an apt process [2].

Concerning the high-energy emission, there is no need to assume coherent emission. Indeed, two main mechanisms are usually considered [23]: (i) synchrotron emission and (ii) curvature emission. First of all, we shall point out some basics features on the radiation emitted by magnetospheric electrons (and positrons), which are responsible for both processes. In an uniform magnetic field B, electrons and positrons move in a spiral orbit which can be decomposed into the sum of a motion parallel to the field line (guiding centre motion) and a circular motion with a cyclotron frequency $\omega = eB/m_e\gamma c$, where e is the charge, B the magnetic field, m_e the mass and $\gamma = \sqrt{1+(p/m_ec)^2}$ is the Lorentz factor. The pitch angle α between the direction of the velocity vector v and the orientation of the field line is constant. Since the particle is gyrating, it is accelerated towards the centre of its orbit and therefore it experiences a radiation loss $-\left(\frac{dE}{dt}\right)$ provided by the formula [10]:

$$-\left(\frac{dE}{dt}\right) = \frac{e^2\gamma^4}{6\pi\epsilon_0 c^3}[|a_\perp|^2 + \gamma^2|a_\parallel|^2] \tag{1.15}$$

where ϵ_0 is the vacuum permittivity, while $a_\perp$ and $a_\parallel$ are the perpendicular and parallel components of the acceleration with respect to the field line orientation respectively. Since the acceleration is always perpendicular to the velocity vector of the particle, $a_\perp = evB\sin\alpha/\gamma m_e$ and $a_\parallel = 0$. Therefore, the total radiation loss rate of the charged particle is [10]:

$$\begin{align} -\left(\frac{dE}{dt}\right) &= \frac{e^2\gamma^4}{6\pi\epsilon_0 c^3}|a_\perp|^2 \tag{1.16} \\ &= \frac{e^4B^2}{6\pi\epsilon_0 c m_e^2}\frac{v^2}{c^2}\gamma^2\sin^2\alpha \tag{1.17} \end{align}$$

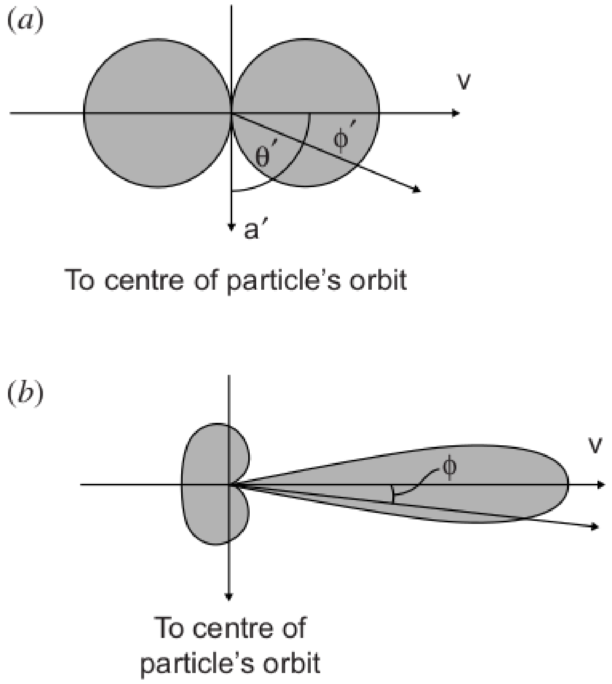

Figure 1.5: Geometry of the synchrotron emission as seen in the electron's reference frame (a) and in the inertial reference frame (b). Figure taken from [10].

We can rewrite this expression using $c^2 = (\mu_0\epsilon_0)^{-1}$, where μ_0 is the vacuum permeability, and introducing the energy density of the magnetic field $U_{mag} = B^2/2\mu_0$ [10]:

$$-\left(\frac{dE}{dt}\right) = 2\sigma_T c U_{mag}\frac{v^2}{c^2}\gamma^2 \sin^2\alpha \tag{1.18}$$

where σ_T is the Thomson cross section given by:

$$\sigma_T = \frac{e^4}{6\pi\epsilon_0^2 c^4 m_e^2} \tag{1.19}$$

This result is valid for an electron (or positron) with pitch angle α. However, for a population of high energy electrons we shall consider a distribution of pitch angles, which is likely to be randomized either by irregularities in the magnetic field distribution or by streaming instabilities [10]. Hence this distribution is expected to be isotropic. By averaging over this distribution, an expression for the average energy loss is obtained [10]:

$$-\left(\frac{dE}{dt}\right) = \frac{4}{3}\sigma_T c U_{mag}\frac{v^2}{c^2}\gamma^2 \tag{1.20}$$

A peculiar characteristic of the synchrotron radiation is the relativistic beaming in the direction of motion of the electron. Let us consider first an electron which is gyrating around the magnetic field line at a pitch angle of 90^o. In the reference frame of the electron, the angular distribution of the intensity of radiation with respect to the acceleration vector is $I_\nu \propto sin^2\theta' \propto cos^2\phi'$, where $\phi' = \frac{\pi}{2} - \theta'$ (Figure 1.5(a)) [10]. Most of the energy is found to be emitted in the range $\frac{\pi}{4} \leq \phi' \leq \frac{\pi}{4}$ and, by considering the relativistic formula for the aberration of light between two reference frames, we get that in an inertial reference frame most of the energy observed is emitted in the range $-\frac{1}{\gamma} \leq \phi \leq \frac{1}{\gamma}$ [10]. Therefore the emission appears elongated and beamed in the direction of motion of the electron (see Figure 1.5(b)).

Finally, let's consider the curvature radiation, which occurs even when the electron has no transverse momentum, so that $p_\perp$=0. In this case, the motion of the electrons can be considered as an instantaneous circular motion with radius R given by the curvature of the field line. Thus the characteristic of the emitted radiation are quite similar to those of the synchrotron radiation.

1.1.5 Spin Evolution

As a matter of fact, all the braking mechanisms we have seen hitherto must give birth to different torques, which will slow down the pulsar relentlessly. We discuss three mechanisms: (i) the electromagnetic torque, (ii) the magnetic stress and (iii) the pulsar wind.

We have already mentioned the electromagnetic radiation emitted by a rotating dipole in section 1.1.1, which we call now electromagnetic spin-down. The rate of energy emitted is $\dot{E} = N_{em}\Omega$, where Ω is the usual angular velocity of the neutron star and N is the torque which will be, using eq.(1.4) [2]:

$$N_{em} = \frac{2}{3}\frac{\mu^2\Omega^3}{c^3} \tag{1.21}$$

with μ being the magnetic moment. Since this torque is of electromagnetic nature, it will occur even in vacuum. It spins the neutron star down from an initial period P_i to a period $P \gg P_i$ within a timescale [2]:

$$t_{em} \approx 3\times10^4\Big(\frac{P}{50\,ms}\Big)^2 I_{45}\mu_{30}^{-2}\ \text{yr} \tag{1.22}$$

where I_{45} is the moment of inertia in units of 10^{45} g cm^2, μ_{30} is the magnetic moment in units of 10^{30} G cm^3.

As we discussed in section 1.1.3, in the astrophysical context we are facing the pulsar is surrounded by plasma, and the effects of this plasma make the spin-down evolution more complex. Besides the electromagnetic torque, the magnetic stress due to the bending of the open field lines will act on the pulsar, leading to a braking mechanism of the same kind of the electromagnetic torque (see section 1.1.3) with a similar timescale.

Finally, we mention the pulsar wind. Following [24], charged particles are accelerated in the collapse of charge-separated gaps either near the pulsar polar caps or in outer regions that extend to the light cylinder. The pulsar wind was first suggested by [22], who modelled this emission mechanism for an aligned rotator. We briefly summarize the main concepts, since their calculations still provide the basis for the modern approach to the pulsar wind [24].

The magnetosphere can be divided into three zones: the near zone (within the light cylinder), the wind zone (which encloses the near zone) and the boundary zone. In the first two zones the magnetic field lines are electric equipotentials, thus the charged particles slide along these field lines [22], which can be at higher, equal or lower electrostatic potential than the interstellar gas which surrounds the pulsar. The critical line (see Figure 1.4) is the magnetic field line where the electric potential equals that of the interstellar gas. Protons and electrons escape along the field lines which are at higher and at lower electrostatic potential than the interstellar gas respectively [22]. Assuming that the magnetic and the rotation axes are parallel, electrons flow along the field lines closest to the poles, and protons escape along the lower-latitude open lines [22]. These streams of particles remain separated until they reach the boundary zone, where they receive most of their acceleration. Indeed, in the boundary zone the magnetic field lines are not equipotential, and charges can move across their poloidal component. The net flow of charged particles steals energy and momentum from the neutron star, which consequently slows down.

1.2 Pulsar Timing

1.2.1 Introduction

As we saw in section 1.1.1, the peculiar feature of pulsars is their signal, which is a repeating pulse occurring with a well-defined period, such as a lighthouse, identified with the rotational period of the neutron star. The shape of the signal varies significantly from pulse to pulse, and in some cases it can even disappear [25] or, on the other hand, abruptly increase. The former event is called nulling: a sudden reduction of the pulse intensity to a $\leq 1\%$ value, and this state lasts for a time interval which varies from some periods to 70% of the time, depending on the pulsar, before returning suddenly to the usual intensity. This phenomenon is thought to be linked with the pulsar aging: as the neutron star

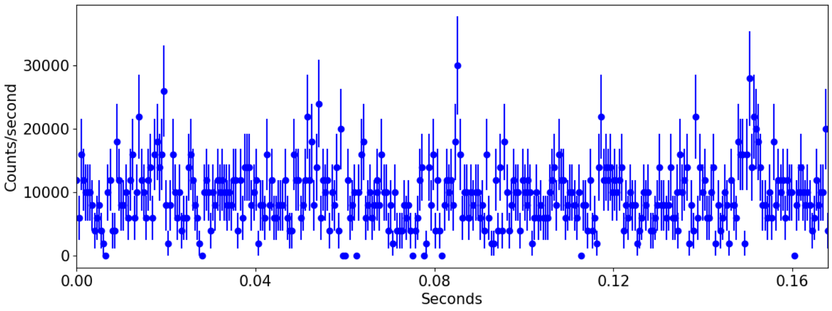

(a)

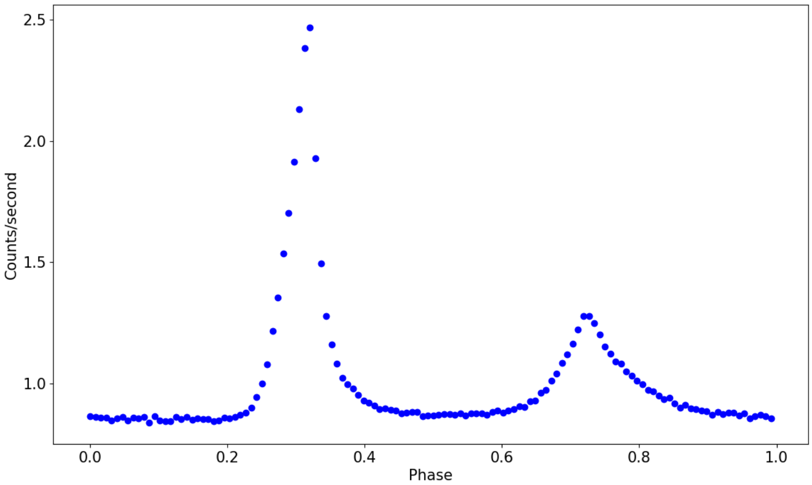

(b)

Figure 1.6: Figure (a): Binned light curve of the Crab Pulsar on 2018 January 1. Counts/second vs time of arrival of each photon (seconds) are shown. The binning time is set to 0.0005 s. Figure (b): folded profile of the Crab pulsar. Normalized counts/second are shown as function of the phase. The integration was done over 5 minutes of observation, taking a rotational period of 0.033744582 s.

ages, the fractional time spent in the nulling state increases, until it approaches 100% and the pulsar crosses the “death line” (see Figure 1.7). On the other hand, a sudden increase is connected to active bursts [26] or Giant pulses [2]: individual pulses which can be hundreds of times brighter than usual.

Even if the single pulse changes, if we integrate over hundreds rotations we will obtain a signal which is remarkably stable (see Figure 1.6 (b)). As a matter of fact, the integrated profile of many pulsars can be used to define a timescale whose stability could compete with that of the atomic clocks [27]. The integrated pulse, or *folded* profile, is usually composed by a main component, which is a smooth peak that occupies only 2-10% of the total period extent, and, in some cases, by an interpulse, which is a weaker peak (Figure 1.6 (b)). However, multi-structures profiles are widely observed.

The reduced width of the main peak could be a clear hint to think the pulsar emission is a process which occurs over a small rotation angle of the pulsar: indeed, the energy flux is above the quiescent flux level only for a small fraction of the rotation period. Some features like the separation between the components can vary when changing the observed wavelength. Thus, the stability of the pulsar shape is defined for each frequency independently. Furthermore, some pulsars show a swinging between two (or more) shapes: at unpredictable (but with a defined order of magnitude) time intervals, the pulse shape changes from a normal, i.e. the one in which the pulsar spends most of its time, to an abnormal mode, and viceversa [28], [29].

The morphology of the pulse is very important because from it we can infer some interesting features about the geometry of the pulsar: for example, if we have a pulse and an interpulse roughly at 180^o, we can imagine that they are produced by the two poles of the magnetized neutron star, having the rotation axis almost perpendicular to the magnetic dipole axis and to our line of sight; on the other hand, a broad pulse which covers the entire period can be interpreted as the emission from one pole, which is slightly misaligned with the rotation axis, both lying almost on our line of sight.

1.2.2 Timing Techniques

The study of the signal received by a neutron star is the first asset that can be exploited to infer the pulsar properties: this research thread is called Pulsar Timing. Let us introduce the basic concept of this technique. For a uniform rotator, each pulse arrives at a fixed time, and the separation between two pulses will not change. We know from section 1.1.1 that pulsars are not uniform rotators since they are spinning down. Thus, the rotational period is expected to increase, and the time separation between two pulses to grow. We can therefore quantify the deceleration looking at the phase: comparing the time of arrival of each pulse with that of a uniform rotator, we can state if the neutron star is accelerating or decelerating. Indeed, if the phase is increasing, every pulse we receive will arrive later than that of a uniform rotator; on the other hand, if the pulsar is spinning up, each pulse will anticipate the uniform rotator. Therefore, a fundamental tool in pulsar timing is the measurements of the Time of Arrival (ToA) of the main peak or, more in general, of a photon, which is done as follows.

First of all, the detection of the signal depends on the wavelength considered. For this work we are dealing with optical light and, as it will be further explained in section 2.2, we used a single photon counting photometer. This detector gives us a time series: whenever a photon is collected, the time at which this event occurs is registered. Therefore, the time series tells us when each photon is detected during the whole observation session. However, this time series is referred to the rest frame of the telescope, i.e. topocentric. We need an inertial frame that we can refer to: this is usually taken to be the Solar System (hereafter SS) rest frame, namely the inertial reference frame centred in the SS barycenter. To do this, we shall introduce the infinite-frequency pulse, defined as the pulse measured at infinity frequency [2]. This concept will be clarified soon after.

Calling t the topocentric ToA and t_b the corresponding barycentric ToA, the delay between them is [2], [30]:

$$t_b - t = \frac{d - |\vec{d} - \vec{r}|}{c} - \frac{D}{\nu^2} + \Delta_c + \Delta_{E_\odot} - \Delta_{S_\odot} \tag{1.23}$$

where $\vec{d} = \hat{n}d$ is the vector distance between the pulsar and the SS barycenter, $\vec{r}$ points from the SS barycenter to the telescope, ν is the frequency of observation, D is the dispersion constant of the pulsar (see below), Δ_c is the offset between the observatory's master clock and the reference atomic standard, $\Delta_{E_\odot}$ and $\Delta_{S_\odot}$ are two relativistic corrections. Let us describe each term. The first term is called the Rømer delay and is due to the different times of propagation of the electromagnetic waves from the pulsar to the telescope and from the pulsar to the SS barycenter due to the orbital motion of Earth around the Sun. Usually the Rømer delay $\Delta_{R_\odot}$ is expressed through a Taylor expansion [2]:

$$\Delta_{R_\odot} = \frac{d - |\vec{d} - \vec{r}|}{c} \approx \frac{\hat{n} \cdot \vec{r}}{c} + \frac{(\hat{n} \cdot \vec{r})^2 - r^2}{2dc} \tag{1.24}$$

The order of magnitude of the Rømer delay is $\frac{P_T}{2\pi} \frac{v_T}{c}$ where P_T is the Earth's orbital period and v_T its velocity with respect to the SS barycenter.

To discuss the second term we shall introduce the dispersion measure (DM) of the pulsar:

$$DM = \int_0^d n_e dl \tag{1.25}$$

where n_e is the electron density, d is the distance and the integration is performed along the line of sight. The DM is therefore the column density of electrons along the line of sight to the pulsar, expressed in cm^{-3}pc. Thus, the term D/ν^2 is the frequency-dispersion of the ToA [2], measured in Hz and related to the DM through:

$$D = DM\Big(\frac{e^2}{2\pi m_e c}\Big) \tag{1.26}$$

where e and m_e are the charge and the mass of the electron respectively. As we can appreciate, this delay scales with ν^{-2}, thus for the aforementioned infinite-frequency pulse measured for $\nu \rightarrow \infty$ it will vanish there.

The relativistic term $\Delta_{E_\odot}$ is called the Einstein delay. It includes the effects of the gravitational redshift and time dilatation due to the motions of Earth and other bodies in the SS. It is calculated from the expression:

$$\frac{d\Delta_{E_\odot}}{dt} = \sum_i \frac{Gm_i}{c^2 r_i} + \frac{v_T^2}{2c^2} - \text{const} \tag{1.27}$$

where the index i is referred to all the bodies in the SS whose masses are non negligible. The mass is indicated with m while the distance with r; the velocity of the Earth with respect to the barycenter of the SS is again v_T. The constant is chosen to make the right hand side of the equation to vanish when averaging for long time. The order of magnitude of the Einstein delay is given by $(e_T v_T)/c$ where e_T is the eccentricity of the Earth's orbit.

The last term is called the Shapiro delay $\Delta_{S_\odot}$. It is an effect predicted by General Relativity. This delay is due to the bending of the light rays which travel near a massive object, since the spacetime is curved. In this case the main source of the Shapiro delay is the Sun. Neglecting the Earth's eccentricity, which is small compared to other terms, the Shapiro delay is given by:

$$\Delta_{S_\odot} = -2T_\odot \log(1 + \cos\theta) \tag{1.28}$$

where θ is the pulsar-Sun-Earth angle at the time of the observation and $T_\odot = GM/c^3$ is a timescale often used in pulsar timing. The Shapiro delay depends on the angular impact parameter θ, and its maximum value of 120 μs is reached when $\theta = 180^o$.

For the Rømer, Einstein and Shapiro's delays the position and the velocity of the telescope on Earth, i.e. the topocenter, are needed. These are determined by firstly interpolating a SS ephemeris, then adding terms that account for measured irregularities in the Earth's rotation.

Finally, the Δ_c term, which is the clock correction, can be obtained from measurements made with the satellites of the Global Positioning System (GPS). The reference to a primary atomic time scales can be made if the offset between this primary time reference and the standard time used during the observations (usually referred to the GPS time) is known.

For isolated pulsar like the Crab, the barycentric time t_b can be expressed as $\mathrm{T} = \mathrm{t_b} - \mathrm{t_o}$ where T is the proper time in the pulsar rest frame and t_o is a (nearly) constant term given by the Doppler shift and the gravitational redshift of the pulsar [2].

Once we have the barycentric ToAs, we can proceed with the timing analysis. First of all, the data must be binned to build the light curve (Figure 1.6 (a)) and, through a power spectrum analysis of the latter, a first estimate of the pulsar rotational period can be made. The light curve is subsequently split into intervals, typically of few hundreds rotations, and then each interval is folded to get an integrated profile, namely a single phase plot which is given by the average of all the rotations occurring in the interval considered. For example, within an observation lasting 30 minutes we can choose intervals of 5 minutes to get 6 folded profiles; each of these folded profiles will look like Figure 1.6 (b).

As explained at the very beginning of this section, we shall parse the evolution of the pulses in order to understand the rotational behaviour. To accomplish this aim, each folded profile is fitted with an appropriate function that provides an accurate representation of the average pulse profile. Then, looking at the position of the main peak in every profile we get an estimate of the acceleration or deceleration of the rotation with respect to the uniform rotator. Indeed, the drift of the main peak position can be fitted with an apt curve, which will depend on some fundamental parameters: this is called the timing solution. The purpose of the pulsar timing is therefore the determination of these parameters.

The pulse phase ϕ(T) can be interpreted as the combination of a deterministic term due to the regular spin down mechanism (emission of electromagnetic radiation, magnetic stresses, emission of charged particles) and a stochastic term ε(T) (referred to as the phase noise). A suitable expression for ϕ(T) is:

$$\phi(T) = \nu T + \frac{1}{2}\dot{\nu}T^2 + \frac{1}{6}\ddot{\nu}T^3 + \varepsilon(T) \tag{1.29}$$

where $\nu = \frac{d\phi}{dt} = 1/\mathrm{P}$ is the rotation frequency of the pulsar and dots over quantities are the time derivatives. Neglecting the stochastic term $\varepsilon(\mathrm{T})$, the evolution of the phase can be compared with the model given by eq.(1.29), where the free parameters are ν,$\dot{\nu}$, $\ddot{\nu}$, and a number of parameters related to the pulsar barycentrization (the pulsar right ascension α and declination δ, its parallax π, the reference epoch t_o, the parameters describing its proper motion $\mu_\alpha = \dot{\alpha}\cos\delta$ and $\mu_\delta = \dot{\delta}$, the dispersion constant D). To determine these parameters we can minimize the difference between the computed ϕ and the observed pulse ϕ_o by means of the χ^2 statistics:

$$\chi^2 = \sum_{i=1}^{N}\Big[\frac{\phi_o(T_i) - \phi(T_i)}{\sigma_i}\Big]^2 \tag{1.30}$$

where N is the total number of ToAs, namely the number of folded profiles, $\phi_o(T_i)$ is the i-th observed main peak position, $\phi(T_i)$ is the fitting eq.(1.29) evaluated at time T_i and σ_i is the uncertainty in the i-th observed main peak position.

If we assume that the period increases due to emission of electromagnetic radiation from a magnetic dipole, combining eq.(1.3) and eq.(1.4) the spin down can be expressed as:

$$\dot{\Omega} = -k\Omega^3 \tag{1.31}$$

where $\Omega = 2\pi\nu = 2\pi/P$ is the rotation angular velocity, k=$(2\mu^2\sin^2\alpha)/(3\mathrm{Ic}^3)$, μ magnetic dipole moment, α the angle between the rotation and the magnetic axes, I the moment of inertia and c the speed of light. We can generalize the spin down equation (1.31) introducing the braking index n:

$$\dot{\Omega} = -k\Omega^n \tag{1.32}$$

The braking index plays a central role in neutron star physics since different processes of rotational energy loss will lead to different values of n. Thus, determining this number provides direct information on the fundamental physics involved [3], [31], [32], [33]. In the simple approximation of k=constant, we can derive the braking index directly from the evolution of the rotational period [10]. Indeed, deriving eq.(1.32):

$$\ddot{\Omega} = -kn\Omega^{n-1}\dot{\Omega} \tag{1.33}$$

and taking the ratio between eq.(1.33) and eq.(1.32) we get:

$$n = \frac{\ddot{\Omega}\Omega}{\dot{\Omega}^2} = \frac{\ddot{\nu}\nu}{\dot{\nu}^2} = 2 - \frac{\ddot{P}P}{\dot{P}^2} \tag{1.34}$$

We can compare eq.(1.34) with the canonical value 3 given for a magnetic dipole braking (see eq.(1.31)): the measured values are systematically lower than 3 [10], thus suggesting the inference of other processes, like non-dipolar components in the magnetic field, the occurrence of particle acceleration in the magnetosphere, free precession of the spin axis or decrease of the magnetic field with time [2]. Therefore, we need more sophisticated models to describe the braking index, and then the energy loss processes involved, which are nevertheless constrained from the timing solution [31]. Unfortunately, a meaningful measurement of n can be done only for young pulsars, since the timing noise due to the aging increases the uncertainties [2].

Another important quantity that we can infer from the timing solution is the characteristic age τ. Integrating eq.(1.32) for $n \neq 1$ between an initial angular velocity Ω_i at t=0 and the current angular velocity we get:

$$t = -\frac{\Omega}{(n-1)\dot{\Omega}}\left[1 - \Big(\frac{\Omega}{\Omega_i}\Big)^{n-1}\right] \tag{1.35}$$

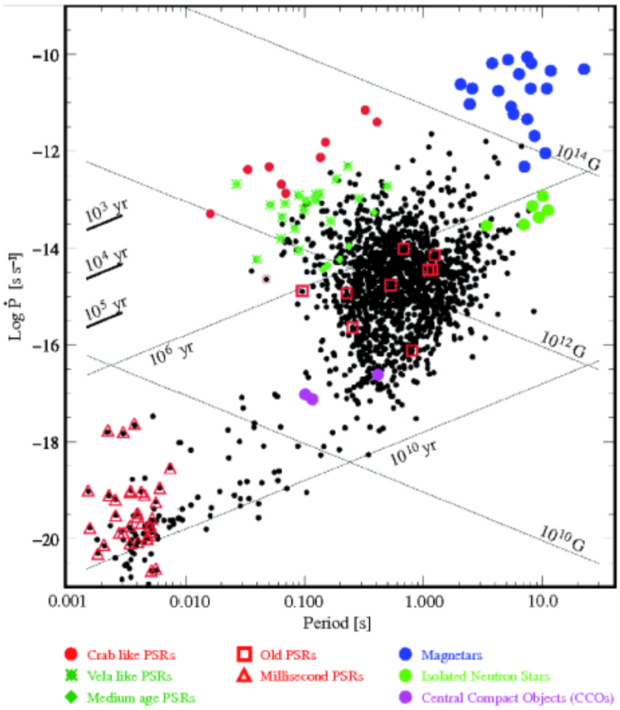

Figure 1.7: P-Ṗ diagram for radio pulsars. Figure taken from [34].

Considering that $\Omega_i \gg \Omega$, the square bracket is ~1 and t becomes the characteristic age, which is an upper limit for the actual age of the pulsar:

$$\tau = -\frac{1}{n-1}\frac{\Omega}{\dot{\Omega}} = -\frac{1}{n-1}\frac{\nu}{\dot{\nu}} = \frac{1}{n-1}\frac{P}{\dot{P}} \tag{1.36}$$

For the Crab pulsar, τ is $\sim$ 1250 yr, but its actual age is $\sim$ 950 yr, obtained from a recorded supernova explosion detected by Chinese astrologers in 1054 AD.

In Figure (1.7), taken from [34], we show the P-Ṗ diagram for radio pulsars [34]. We can see that the pulsars are clustered in two main groups: one at slow rotation rate, i.e. P $\sim$ 0.1-1 s, and high spin down rates, Ṗ $\sim$ 10^{-13}-10^{-16} s/s; the other at fast rotation rates with P $\sim$ 1-10 ms and low period derivatives, Ṗ $\sim$ 10^{-19}-10^{-20} s/s. The former is identified as the group of young pulsar at an early stage of their lives, while the latter includes old neutron stars which have been spun up by mass accretion in binary systems [2].

To conclude this section, let us consider the term $\varepsilon(T)$ in eq.(1.29), which contains the irregular period phase changes called noise. They appear as "residuals" after subtracting the best fitting regular spin down law. These residuals are due to (i) timing noise, which is a noisy, random evolution of the phase, and to (ii) sudden increases in the angular velocity of the neutron star, the so-called Glitches. The physical origin of the timing noise is currently debated. It could be caused by random walk behavior of the phase, the frequency and the spin-down rate, which are called phase, frequency and derivative noise respectively [2]. However, recent works suggest that such a simple model cannot reproduce the timing irregularities observed [35]. Concerning phase noise, in [2] it is suggested that a jitter of the emission spot around a mean position on the pole of the neutron star could be a feasible explanation. Similarly, a fluctuation of the rotation frequency and the spin-down will cause frequency and derivative noise respectively. The former can be, for example, a fluctuation in the coupling between the solid crust of the neutron star and the underlying superfluid (see section 1.1.2), whereas the latter can be due to fluctuations in the magnetic field structure of the pulsar [2]. It is very likely that all these phenomena occur simultaneously. In a young and active pulsar like the Crab, other phenomena need to be considered: a high-order period derivative hiding in the timing noise or low frequency oscillations which cause a quasi-periodic behavior of the noise [2]. Concerning glitches, we will extensively analyze this phenomenon in section 2.1.

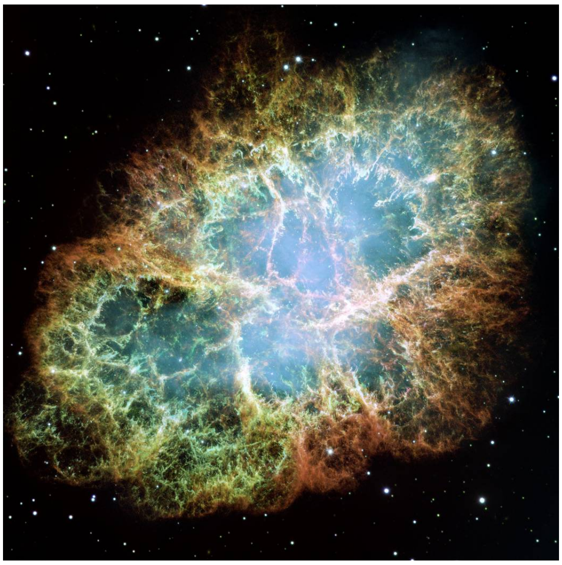

Figure 1.8: The Crab Nebula observed by the Hubble Space Telescope. Image credit: NASA, ESA, J. Hester, A. LoLL (ASU).

1.3 The Crab Pulsar

1.3.1 Introduction

The Crab pulsar (PSR B0531+21) is the central neutron star of the Crab Nebula (Figure 1.8). Its formation dates back to the supernova SN1054 explosion, recorded by Chinese astrologers on 1054 July 4, who reported that a “guest star” was visible for three weeks during the daytime and for 22 months at night [36]. In 1731 the Crab nebula was (re)discovered by the English astronomer John Bevis, and it was subsequently observed in 1758 by Charles Messier, who introduced it in his catalog of nebulous non-cometary object (M1). The nebula was named "Crab" by the Irishman William Parsons in 1850 [36]. The link between the Crab nebula and the the supernova SN1054 was first suggested by [37] in 1921. The relation was then corroborated by Hubble in 1928 [38], who used the expansion velocity of the nebula to trace back the supernova event. The turning point came in 1942, when [39] and [40] provided a complete study of modern observations of the expanding nebula and of the early Chinese records: this work unambiguously confirmed that the Crab nebula is the remnant of SN1054 [36]. In 1967 Pacini proposed that the nebula is powered by a highly magnetized, fast rotating neutron star at the centre of the nebula itself [20]. In 1968 Gold confirmed this hypothesis by comparing the observed bolometric luminosity of the nebula with the computed rate of loss of rotational energy by the central neutron star [1]. In 1968 the neutron star was finally discovered at radio wavelengths [41], [42] and it was subsequently observed at visible wavelengths [43], becoming the first pulsar detected in this band.

1.3.2 The Structure of the Crab Nebula

In Figure 1.9 we show the structure of the Crab nebula as presented in [36]: moving from the centre outwards, the Crab nebula consists of (i) the Crab pulsar, (ii) the Crab synchrotron nebula, (iii) an expanding shell of thermal gas and (iv) a freely expanding supernova remnant [36]. We provide a brief summary of these components and we refer to [36] for further detailed information:

- The Crab pulsar is the neutron star located at the centre of the Crab nebula. Thanks to its proximity of $\sim$ 2 kpc [44], it is probably the most studied pulsar: it has been monitored regularly in the radio wavelengths since its discovery in 1968 [3]. Besides, it is the brightest (V$\sim$16.6 mag) neutron star in the optical domain, giving an insight on the geometry of the emission regions by comparing the time behaviour in different bands [4].

  The Crab pulsar has a rotational frequency $\nu \sim$ 30 Hz (or, equivalently, a period P $\sim$ 33 ms), and a frequency derivative $\dot{\nu} \sim$ -3.77 $\times$ 10^{-10} Hz/s [3]. Assuming that the star is a uniform sphere

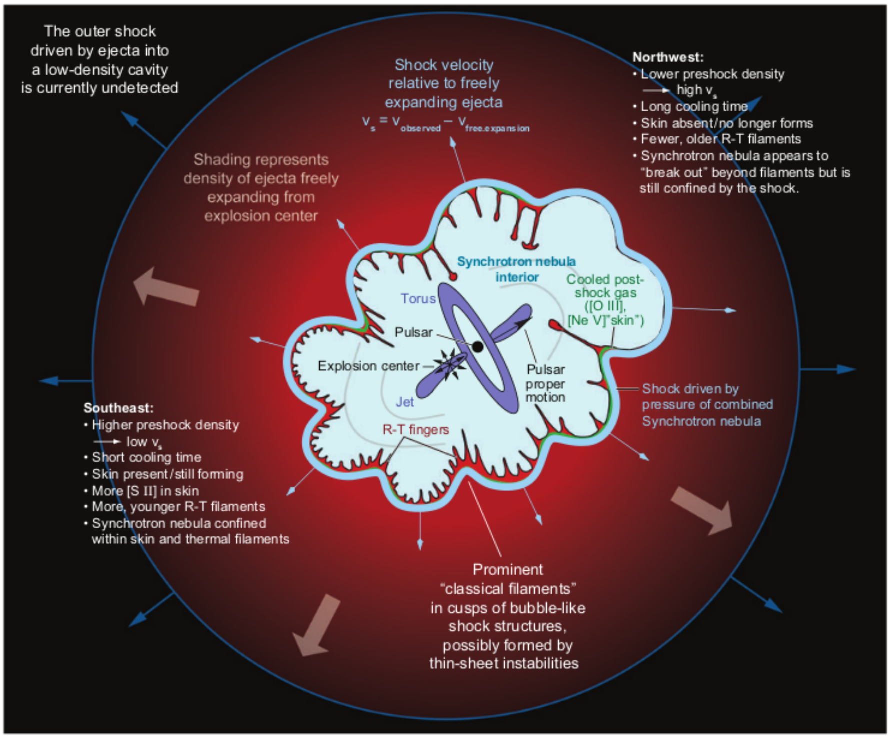

Figure 1.9: Schematic view of the structure of the Crab nebula. Figure Taken from [36].

with a radius of 10 km and a mass of 1.4 $M_\odot$, the moment of inertia of the pulsar is $I = 1.12 \times 10^{45}$ g cm^2, and the spin-down luminosity is $L = 4\pi^2 I\dot{P}P^{-3} \sim 5 \times 10^{38}$ erg/s, or 130000 $L_\odot$ [36].

As explained in section 1.1.4, only a small fraction of this spin-down luminosity goes into the pulsed emission we detect. The majority of the emitted energy is carried away by the magnetic dipole radiation and the ultrarelativistic wind [36].

- The Crab synchrotron nebula which surrounds the pulsar is a structure which fills an ellipsoidal volume with a major axis of 4.4 pc and a minor axis of 2.9 pc, tilted into the plane of the sky by 30^o [36]. The features of the synchrotron nebula, called wisps, are extremely dynamic. A wind shock is found at the inner boundary, between the pulsar wind and the synchrotron nebula. On the other hand, a second shock is found at the outer surface, between the synchrotron nebula and the surrounding thermal gas.

- The thermal gas is a filamentary structure composed of ejecta from the supernova. These filaments are driven by Rayleigh-Taylor instabilities arising between the thermal gas and the inner synchrotron nebula. The expansion velocity of this component ranges from 700 to 1800 km/s [36].

- The freely expanding ejecta from the supernova are located outside the visible edge of the nebula. A possible shock could lie at the outer edge of this expanding cloud.

1.3.3 The Emission of The Crab Pulsar

The Crab nebula and its pulsar show a strong emission throughout the electromagnetic spectrum (see Figure 1.10 (a) taken from [44]). The spectral energy distribution of the Crab nebula peaks in the UV, while the emission from the Crab pulsar peaks in the X-ray band [44]. The energy output of the nebula is a factor ~ 10 larger than that of the pulsar. As explained by [44], the emission of the nebula from radio to X-rays is due to synchrotron emission, while at higher energies (~ 400 MeV), the same electrons produce a second emission component through Inverse Compton scattering. The synchrotron emission from the nebula has an integrated luminosity of $\sim 1.3 \times 10^{38}$ erg/s, which is $\sim 26\%$ of the bolometric luminosity injected into the nebula by the pulsar. A bump at $\sim 10^{13}$ Hz can be seen in the

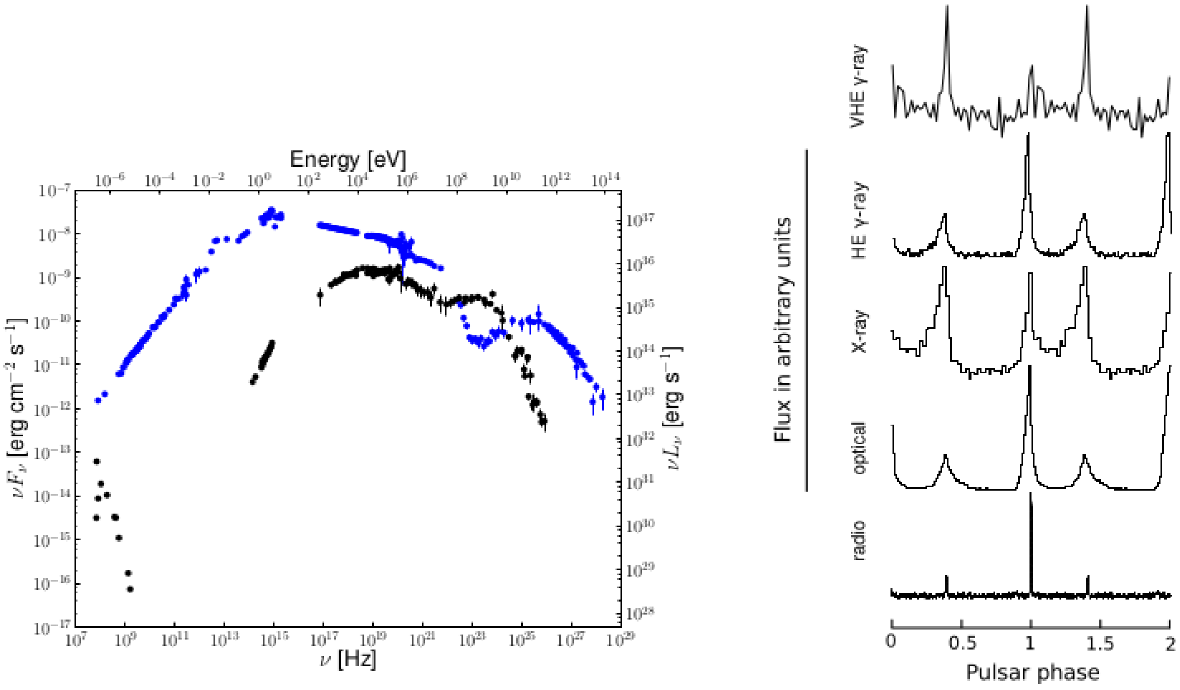

(a)

(b)

Figure 1.10: Figure (a): spectral energy distribution of the average emission of the Crab nebula (blue) and the phase averaged emission of the Crab pulsar (black). On the right axis the luminosity calculated assuming a distance of 2 kpc is shown. Figure (b): Pulse shape at radio (1.4 GHz), optical (1.5 - 3.5 eV), X-ray (100 - 200 keV), High Energy gamma-ray (100 - 300 MeV) and Very High Energy gamma-ray (50 - 400 GeV) energies. Figures taken from [44].

far infrared due to the thermal emission from heated dust [36]. Concerning the pulsar, as discussed in section 1.1.4 the radio emission is provided by a coherent emission mechanism. The optical, the UV and the X-ray emission is incoherent synchrotron radiation. Finally, the γ-ray emission is curvature radiation [45].

The pulsating signal we detect is due to the passage of the beamed emission from the poles across our line of sight, producing a lighthouse effect. The folded pulse shape of the Crab is quite prototypical: as shown in Figure 1.6 (b) for the optical band, it is composed by a main peak and an interpulse separated by a phase of $\sim$0.4. A faint precursor to the main peak is detected at radio frequencies [44] (see figure 1.10 (b)). In the optical, X-ray and γ-ray bands a bridge emission can be seen between the main pulse and the interpulse [45]. The pulses at different wavelengths are not aligned, with the optical, the X-ray and the γ-ray main peaks leading the radio one. We will further discuss this time delay in section 3.3. Finally, the emission in the radio and in the optical bands is polarized, with the position angle PA of the linearly polarized component varying with the pulse phase and with the frequency. In the optical wavelengths, the polarization angle swings from PA $\approx 40^o$ to PA $\approx 170^o$ during the main peak and from PA $\approx 90^o$ to PA $\approx 180^o$ during the interpulse [44].

Since 1970's many efforts have been undertaken to reproduce the rotational evolution using a polynomial as in eq.(1.29), considering as initial frequency ν a value of $\sim$ 30 Hz. Although the braking index varies, it turns out to be $\sim$ 2.5, which may be attributed to a combination of a secular increase in the angle between the rotation and the magnetic axes and a wind torque [3], [31]. Variations of the braking index may be induced by some external instabilities which vary the configuration of the electromagnetic field on large scales and the currents in the plasma within the nebula [32]. Albeit the folded profile is very stable, the regular behaviour is interrupted by small and unexpected spin-up events at which the frequency suddenly increases, i.e. the pulsar rotates faster. This event is called *glitch* and is usually followed by a recovery to the pre-glitch frequency. We further discuss glitches in section 2.1. For the Crab, during a glitch the frequency increases by a small step $\Delta\nu$ of the order of $\nu \sim 10^{-9}\nu$ to $10^{-7}\nu$ [3]; moreover, a possible correlation between glitch amplitude and the time since the last glitch occurred was suggested by [46].

Finally, the Crab pulsar is also known to produce individual pulses that are hundreds of times brighter than usual in the radio domain. These events are called Giant pulses, and in this case can reach energies up to $\geq 2000 < E >$, where $< E >$ is the mean energy of the pulses. The Giant pulse is broadband, so that it occurs at every radio frequency with almost identical features, and it is considered to be related to the intensity of the magnetic field at the light cylinder [2].

Chapter 2

The November 2017 glitch

2.1 Introduction

Since pulsar timing is a high-precision technique, we can detect the small perturbations affecting long term rotational evolution of the neutron star. As anticipated in section 1.2.2, there are two types of timing irregularities, namely timing noise and glitches, which are widespread [35]. Even if recent investigations suggest that they could be strongly related to each other [35], [32], this topic is still highly debated [47].

In this section we focus on the glitch phenomenon, which is an abrupt increase in the rotational frequency ν, namely a spin up event with a very short duration. This step-like jump of the pulse frequency is often followed by an exponential recovery in which ν decays towards the pre-glitch value (Figure 2.1). The analysis of glitches is a powerful tool: according to the most widespread interpretations, these events can provide information on the interior structure of the neutron stars, which could not be investigated through other methods [13]. There are two main theories which invoke an internal origin for glitches: starquakes [2] and the pinning-unpinning model [48].

Let us consider starquakes first. After the Supernova explosion, a solid crust rapidly forms thanks to the neutrino cooling, i.e. the emission of neutrinos from the collapsing core of the star. Since the neutron star is fast-rotating, the shape of the crust will be oblate. As the pulsar slows down, the balance between centrifugal and gravitational forces makes the shape more spherical and less oblate. Conversely, the rigidity given by Coulomb forces tries to maintain the original shape. The opposite action of these forces produces a stress σ, which increases as the pulsar slows down. When the stress exceed a critical value σ_c, the crust suddenly cracks, similarly to earthquakes on Earth, reducing its oblateness. The crustal moment of inertia I_c will then decrease, and so will do the whole moment of inertia of the star I. The angular momentum $L = I\Omega$ must be conserved during this very short event, since braking mechanisms act on timescales of 10^5-10^6 s. The angular velocity Ω must therefore increase and the net effect of the starquake will be a sudden spin up of the neutron star, followed by a relaxation towards pre-glitch values until the stress reaches again the critical value and triggers another starquake. This model seems to work for Crab-like pulsars, predicting a repetition timescale $t \sim$ 10-200 days, which is consistent with the observations [2]. However, the energy stored in the crust is too tiny to explain the rates of the large Vela-type glitches: indeed, the repetition timescale of these glitches would be $t \sim 920$ yr (and thus glitches would be a rare phenomenon), while in the 12 years after its discovery 4 glitches were detected, so $t \sim 3$ yr [2]. The starquakes model could be improved by considering a high shear modulus inside the core due to a quark condensate [48], which would decrease the inter-glitch interval and would possibly strengthen the glitch, but further work is needed. Hence starquakes can account for small glitches but are ineffective for the large Vela-type glitches, the latter being the majority.

Concerning the pinning-unpinning model, let us consider first the structure of the neutron star. The magnetosphere provides the torques which slow down the outer crust and the field lines are anchored to it. However, the inner superfluid is decoupled from the crust since the frictional forces acting between them are supposed to be very small. Thus, while the crust is decelerated, the inner superfluid keeps rotating faster and a velocity lag sets in between the two layers. During a glitch, the angular momentum is transferred from the inner superfluid to the crust and the velocity lag decreases, leading to the spin

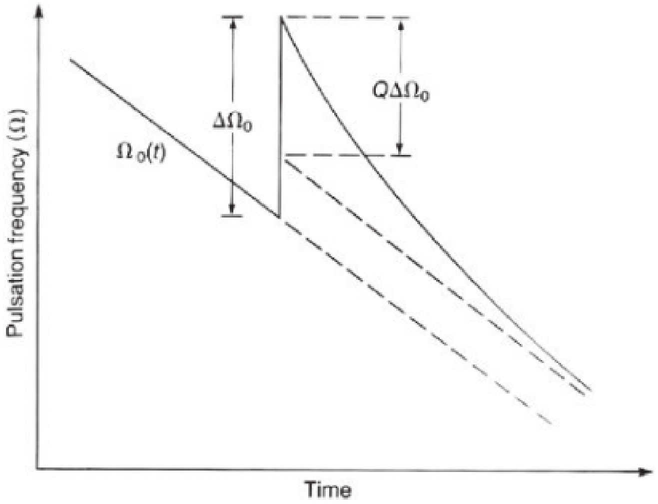

Figure 2.1: Schematic representation of a glitch event. The overall decrease of the angular velocity Ω of the pulsar is interrupted by a sudden spin up event ($\Delta\Omega_0$), which is subsequently followed by a recovery to a value which is slightly larger than the pre-glitch one. Figure taken from [10].

up of the crust. Nevertheless, how can the angular momentum be transferred if there is no frictional force? The answer lies in the properties of the superfluid: (i) on a macroscopic scale, the superfluid is irrotational, i.e. $\nabla\times$ v=0, where v is the fluid velocity; (ii) the angular velocity is quantized, so that in the lowest energy state it is given by $\oint \mathrm{v}\cdot \mathrm{dl} = \mathrm{h}/2\mathrm{m}_n$, where h is the Plank constant and $2\mathrm{m}_n$ is the mass of a neutron pair [10]. These properties mean that the rotation of the neutron fluid is the sum of discrete vortices rotating parallel to the rotation axis. In the Crab Nebula Pulsar the number of vortices per unit area is about 2×10^9 m^{-2}. It is indeed the interaction between these vortices and the crust which allows the transfer of angular momentum: the vortices are pinned to nuclei or to the magnetic flux tubes in the crust, providing the connection between the two layers. The superfluid cannot lose vorticity, lagging behind the proton fluid (that forms a type II superconductor) which instead spins down along with the crust: the relative motion induces a Magnus force between the superfluid and the crust [48]. As the crust slows down, the Magnus force increases until it reaches a critical value which cannot be sustained by vortices, which are forced to unpin and migrate outwards, transferring the angular momentum to the crust. This unpinning can occur in a jerky process, which leads to small glitches, or, on the other hand, there could be a catastrophic unpinning of the vortices, which excites a giant glitch [13].

All things considered, as suggested by [49] we can use crust rearrangements, quakes or crack growing models for Crab-like pulsars, while we can use the pinning-unpinning model for low spin-down rate pulsars. According to this scenario, the authors consider two possibilities: (i) there are different types of pulsars or (ii) the change in the physical trigger of the glitch is due to the aging [49]. In any case, the analysis of glitches can provide a tool to study the interaction between different components within the neutron star. We give a brief summary on the main features of these events:

- the sudden increase in the rotational frequency is usually not resolvable, and the exponential recovery has a typical timescale of 10 to a few hundred days;
- the presence of a feasible minimum size, which may imply a threshold for the trigger of the glitch [47];
- no change of pulse profile or flux density associated with a glitch was observed in a normal radio pulsar so far [46],[49];
- the distribution of the observed glitches as function of their size $\Delta\nu/\nu$ is bimodal [49]: the Vela-like pulsars show glitches with $\Delta\nu/\nu \sim 10^{-6}$, while the Crab-like pulsars' glitches are smaller, i.e. $\Delta\nu/\nu \sim 10^{-9}$ - 10^{-7};

- associated with the glitch, usually there is a linear increase in the magnitude of the spin-down rate $-\dot{\nu}$ (or a decrease in $|\dot{\nu}|$) by an amount $-\Delta\dot{\nu}$, which usually extends from the end of the initial recovery until the next glitch event [50]. Observed values for $\Delta\dot{\nu}/\dot{\nu}$ range from 10^{-3} to 10^{-2};

- on the P-$\dot{\mathrm{P}}$ diagram (Figure 1.7), glitches are more frequent in young pulsars with large spin-down rates [49], and they are larger for higher rotation frequencies;

- even if the most accepted model for glitches is the interaction between the interior layers [50], good results were obtained by modelling timing irregularities as a product of the interaction between the pulsar and its surrounding environment [32];

- the correlation between the glitch amplitude and the time since the occurrence of the previous glitch is still highly debated, with some authors claiming that the distribution of inter-glitch intervals is in agreement with a random process [33], and others supporting the existence of a correlation [46];

- sometimes a glitch can be followed by a delayed spin up, so that a further increase in the rotational frequency occurs after the usual step increase [46].

To conclude this section, we mention that pulsar timing can be exploited to study the spatial configuration of the magnetosphere surrounding the neutron star and/or the geometry of the emission regions. Since the main pulses are not aligned at different wavelengths, we can parse the signal in different bands to constrain the relative positions of the emission regions. We will further discuss this topic in section 3.3.

Free precession of the spin axis can be a possible spatial rearrangement: a phenomenon which, in turn, causes the angle between the rotation and magnetic axes of the neutron star to change periodically in time. It is well known that any free precession would be damped by the internal superfluid ([51] and [52]); however, there is a puzzling evidence for the free precession in the long term cyclical variations of the spin ([53], [54] and [55]), which cannot be fully explained. Albeit we still lack a comprehensive theory which could take into account this effect, the evolution of the inclination angle between the rotation and the magnetic axes towards a value of $\pi/2$ was suggested to cope with the change of the pulsar energy loss: indeed, since the emission mechanisms depend on this angle and assuming that the energy loss tends to a minimum value as the neutron star ages, the inclination angle will change accordingly [56]. Furthermore, the variation of the magnetic axis was recently invoked to explain the observed braking index of the Crab pulsar [31].

Indeed, the purpose of this thesis is to search for evidence of changes in the geometry of the emission region and/or in the magnetosphere of the Crab pulsar possibly induced by the glitch [57].

2.2 IFI+Iqueye

Before describing the data analysis, we shall introduce the instrumentation used to perform the observations of the Crab pulsar used in this thesis. We used the fast photon counter Iqueye [6] mounted at the Galileo Telescope (Asiago, Italy) via a dedicated optical fiber interface (IFI) [58]. Iqueye can record the arrival time of each single photon with high accuracy, similarly to what is usually done in High Energy Astrophysics. A schematic view of the Iqueye design is given in Figure 2.2(a), taken from [6].

The incoming light reaches a holed mirror located at the entrance of the instrument. The light outside the hole is reflected by 90^o and is collected by a field camera, while the light from the target passes through the hole and is subsequently collimated by two lenses. After these lenses, two filter wheels are inserted to select different types of filters or polarizers; nevertheless, for this thesis we used white light. Then, the light is focused through another lens system which, together with the previous lenses, reduces the collected image by a 1/3.25 factor. To limit the field of view of the target a pinhole is inserted. The diameters of the available pinholes are 200, 300 and 500 μm, providing a field of view of 1 to 6 arcseconds.

The light passing through the pinhole impinges on a pyramid with four surfaces which divides the incoming beam into four perpendicular sub-beams. Each of them is subsequently collimated and focused again, to reduce the image by a further 1/3.5 factor. Finally, the focused sub-beams reach four different single photon avalanche photodiodes (SPAD) silicon detectors. For our purposes, the counts collected from the SPADs were summed together and the polarization coming from the four faces was averaged out. The splitting of the beam into four sub-beams has an important advantage: it partially overcomes the problem of the SPAD dead time [6]. Indeed, after the detection of one photon, the SPAD is insensitive to other photons for 75 ns. This dead time, which strongly limits the measured statistics, can be reduced using four different SPADs in parallel, since many photons that would be otherwise lost are collected.

Whenever a photon is detected, the SPADs produce a pulse which is subsequently collected by the acquisition system. The task of this system is to assign an accurate absolute time tag to each event, and store this information into an external memory. This is the most innovative characteristic of Iqueye: the clock of the system is a rubidium oscillator disciplined with a GPS receiver. Each time tag of a photon is referenced to the Coordinate Universal Time (UTC) with an accuracy better than 0.5 ns over one hour of observation [4]. Therefore, the Iqueye system output is a time series, namely a collection of arrival times.

In order to connect Iqueye to the Galileo telescope, a dedicated optical bench was installed at the telescope lateral focus and connected to Iqueye by means of an optical fiber [58]. Indeed, this solution has the advantage to maintain Iqueye in a separate room under controlled temperature and humidity conditions, thus reducing potential systematics related to varying ambient conditions [58]. Furthermore, it facilitates the mounting of the instrument. The optical fiber is part of an independent instrument, the Iqueye Fiber Interface (IFI) [7]. In Figure 2.2(b) from [7] we show the optical design of IFI: after the telescope focus, the incoming beam is collimated through an achromatic lens doublet (I1) and then focused on the optical fiber (OF) with a second achromatic doublet (I2). A beam splitter (I3) is inserted in the collimated portion of the beam. S1, S2 and S3 are the corresponding opto-mechanical supports, and OC is the fiber connector. I3 reflects 8% of the incoming light towards a field camera (FC), and transmits the remaining 92% to the optical fiber. The focal lengths of the two doublets are f1 = 200 mm and f2 = 100 mm, leading to an overall demagnification of 1/2. The core of the optical fiber has a diameter of 365 μm, that corresponds to 12.5 arcsec. The image of the field camera has a plate scale of 62.3 arcsec/mm and a field of view of 11.8×7.4 arcmin^2. Filters can be inserted between I1 and I3. Finally, the light injection from the fiber into Iqueye is realized by means of a dedicated opto-mechanical module (module Z), that acts as a focal multiplier. The module is placed in front of Iqueye and is properly centered and focused. The magnification of this module is 2.5 [7]. The image of the fiber core at the instrument entrance focus is a spot with a size of 912.5 μm, significantly smaller than the diameter of the central hole of the Iqueye entrance mirror [7].

2.3 Observations, Data Reduction and Analysis

Until 2017 the Crab Pulsar was known to produce glitches with a spin frequency increase of $10^{-9} \leq \Delta\nu/\nu \leq 10^{-7}$. However, around MJD 58064 (8 November 2017), the Crab experienced what is now confirmed to be the largest glitch ever detected: the magnitude of the step increase was $\Delta\nu/\nu = 0.516 \times 10^{-6}$ in the radio band, which is more similar to the usual glitches occurring in the Vela-like pulsars than those previously experienced by the Crab [46]. No change of the pulse shape or flux associated with the glitch was observed. This event has been deeply investigated in the radio wavelengths, but a complete analysis in the optical domain has not been undertaken hitherto. In this work we parsed the observations taken around the glitch with IFI+Iqueye mounted at the 122 cm Galileo Telescope in Asiago (Italy) (see Table 2.1 for the geocentric coordinates). In Table 2.2 we list the performed observations, divided into three observing runs: October 4 and 7, November 17 and 18, December 30. All of them were carried out in white light.

The raw data were first reduced referring them to UTC. Then, as explained in section 1.2.2, the topocentric time series acquired was converted to an inertial reference frame at the SS barycentre. The conversion was performed using the `TEMPO2` pulsar-timing package, which provides a precision of ~ 1

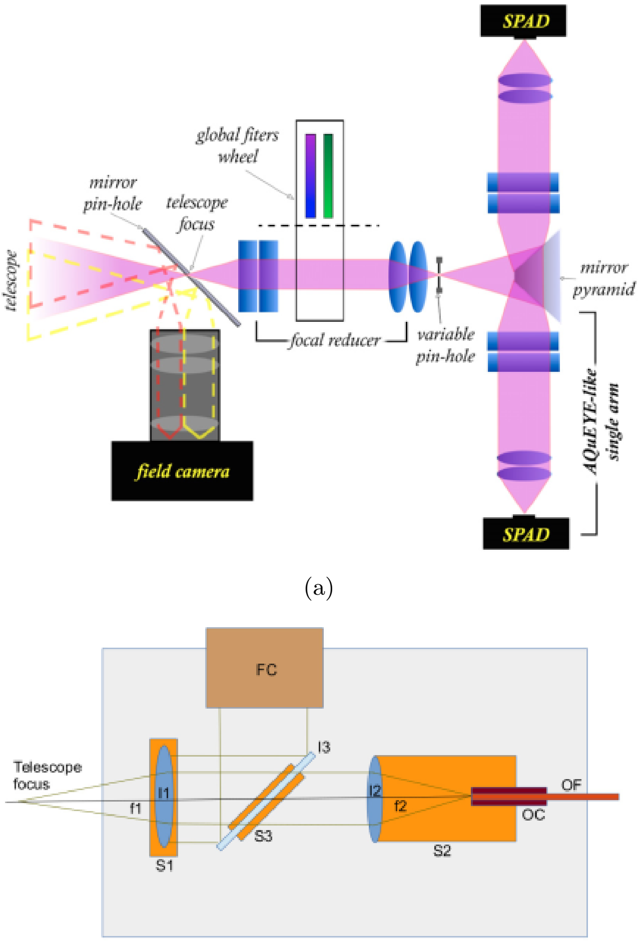

(a)

(b)

Figure 2.2: Figure (a): schematic view of the optical design of Iqueye, taken from [6]. Figure (b): schematic view of the optical design of IFI taken from [7].

ns. We refer to [59] and [60] for a detailed description. The transformation introduced in eq.(1.23) is performed as follows:

$$\Delta t = \Delta_c + \Delta_A + \Delta_{E_\odot} + \Delta_{R_\odot} + \Delta_{S_\odot} - \frac{D}{\nu^2} + \Delta_{VP} + \Delta_B \tag{2.1}$$

where Δ_c is the clock correction, Δ_A is the atmospheric propagation delay, $\Delta_{E_\odot}$ is the SS Einstein delay, $\Delta_{R_\odot}$ is the SS Rømer delay, $\Delta_{S_\odot}$ is the SS Shapiro delay, D/ν^2 is the frequency dispersion of the ToAs, Δ_{VP} is the excess vacuum propagation delay due to secular motion and Δ_B contains the term related to dual source orbital motion (which is null in this case since the Crab is not in a binary system) [59]. The Δ_{VP} term includes the secular motion of the pulsar with respect to the SS barycentre, which affects the timing measurements through the Shklovskii effect [61]. Furthermore, it affects the radial velocity and the radial acceleration, which have a direct impact on the spin and on the spin derivative respectively [59]. Finally, the secular motion can lead to a mixing of the radial velocity into the Shklovskii term, affecting the spin period second derivative [59].

2.3.1 Phase Period Search

After the barycentrization, we binned the time series to get the light curves of the Crab pulsar, which directly provided a first estimate of the available statistics. In Figure 2.3 we show two intervals of the light curves obtained from QEYE_20171004-040731_crab (Figure (a), October 4) and QEYE_20171118-024151_crab (Figure (b), November 18), which are representative for the highest and the lowest available statistics respectively. The binning time is set to 0.001 s for both the light curves. On October 4, the

x (m)	y (m)	z (m)
4360008.516	889148.476	4555709.153

Table 2.1: Geocentric coordinates of the Galileo Telescope in Asiago (Italy).

Observation ID	Start time (UTC)	Start time (MJD)	Duration (s)
QEYE_20171004-040731_crab	October 4, 02:11:29.024	58030.09130814821803	1798
QEYE_20171004-044947_crab2	October 4, 02:53:45.586	58030.120666505427298	1198
QEYE_20171007-023001_crab	October 7, 00:34:22.798	58033.023874981727694	898
QEYE_20171007-024554_crab2	October 7, 00:50:16.889	58033.034917699467936	898
QEYE_20171007-030251_crab3	October 7, 01:07:13.985	58033.046689640844843	898
QEYE_20171007-032212_crab4	October 7, 01:26:34.093	58033.060116815182024	898
QEYE_20171007-033808_crab5	October 7, 01:42:30.508	58033.071186432525224	898
QEYE_20171007-035634_crab6	October 7, 02:00:56.340	58033.083985414596825	898
QEYE_20171007-041250_crab7	October 7, 02:17:12.651	58033.095285308652567	898
QEYE_20171007-044815_crab9	October 7, 02:52:37.577	58033.119879362838038	898
QEYE_20171007-050700_crab10	October 7, 03:11:22.759	58033.132902299343076	898
QEYE_20171007-052333_crab11	October 7, 03:27:56.038	58033.144398590273944	898
QEYE_20171007-054303_crab12	October 7, 03:47:25.928	58033.15793897624485	898
QEYE_20171117-014607_crab	November 17, 00:54:52.094	58074.038102943087441	898
QEYE_20171117-020455_crab	November 17, 01:13:39.151	58074.051147582685303	898
QEYE_20171117-023605_crab	November 17, 01:44:49.575	58074.072796008558207	898
QEYE_20171117-031600_crab	November 17, 02:24:44.357	58074.10051338715644	898
QEYE_20171118-024151_crab	November 18, 01:50:40.367	58075.076856099507012	1798
QEYE_20171118-033311_crab	November 18, 02:41:59.711	58075.112496650025477	1798
QEYE_20171230-235440_crab	December 30, 23:04:08.465	58117.961209086285322	1798
QEYE_20171231-003758_crab	December 30, 23:47:26.721	58117.991281496316642	1798
QEYE_20171231-011907_crab	December 31, 00:28:35.598	58118.019856460156944	1798

Table 2.2: Log of the observations of the Crab nebula pulsar, taken with Iqueye mounted at the 122 cm Galileo Telescope in Asiago. Times are referred to barycenter of the Solar System.

average count rate is 4617 counts/s; on the other hand, the average count rate on November 18 is 3309 counts/s.

The first step of the analysis is determining the rotational period for each observing run. This is needed to fold the time series. The choice of a period strongly influence the final folded profile: indeed, if we fold a time series with a random period, the different rotations of the pulsar will be averaged out and the folded profile will be nearly constant, with a dispersion around a central value which corresponds roughly to the mean of the counts over one rotation; on the other hand, if we take an accurate period, the folded profile will deviate from a constant value, since the contributions from each rotation are summed together in phase. To this end, we used the Fourier analysis, which allows the decomposition of a function into a series of sine and cosine waves, i.e. the Fourier series:

$$f(t) = \frac{1}{N}\sum_{l=1}^{N} a_l e^{-i\omega_l t} \tag{2.2}$$

where ω_l are the Fourier frequencies and a_l are the Fourier coefficients:

$$a_l = \frac{1}{N}\sum_{j=1}^{N} f(t) e^{i\omega_l t_j} \tag{2.3}$$

$e^{\pm i\alpha} = \cos\alpha \pm i\sin\alpha$ is the usual Euler's notation and N is the number of Fourier components

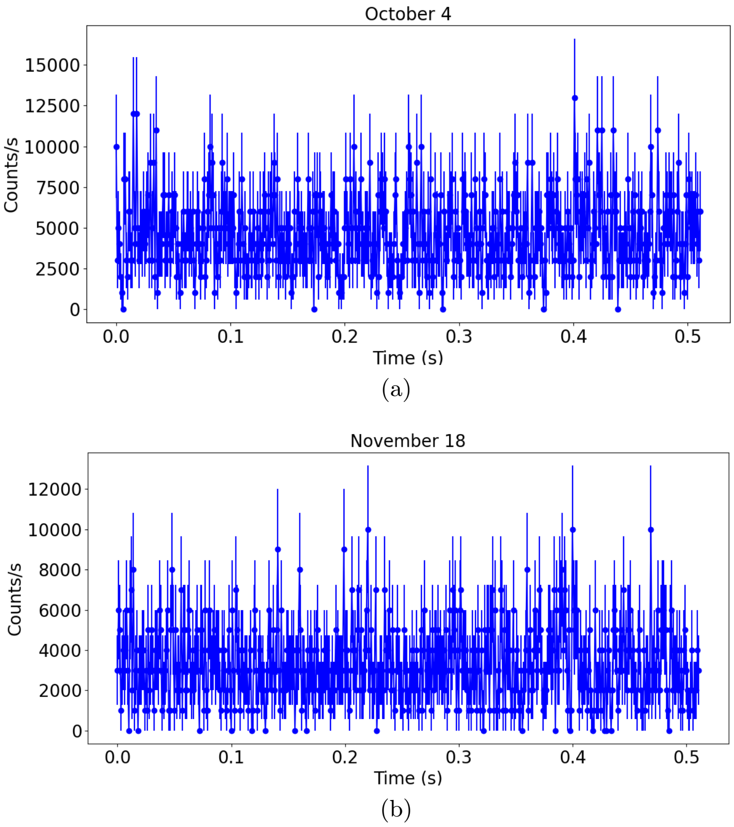

(a)

(b)

Figure 2.3: Figure (a): light curve of 2017 October 4. The start time is 02:11:54 UTC and the average counts/s value is 4617. Figure (b): light curve of 2017 November 18. The start time is 01:51:05 UTC and the average counts/s value is 3309. The binning time is set to 0.001 s for both the light curves.

needed to reproduce the signal. We shall highlight that we deal with discrete functions (the binned light curves), so we do not need the continuous (or integral) form for the Fourier transform. This analysis provides the coefficient a_l which is the amplitude of the l-th wave, namely its "weight" in the function $f(t)$: the bigger the coefficient is, the more important the component is in $f(t)$. From the Fourier components it is possible to construct the power spectrum, namely the $|a_l|^2$ power values as function of the frequency $\nu_l = \omega_l/2\pi$. We show the power spectrum of October 4 and November 17 in Figure 2.4. The fundamental frequency of the power spectrum provides the rotational frequency of the pulsar ν_p.

We performed a power spectrum analysis for each time series using `powspec` from the Xronos software package [62], provided by [63]. This software makes use of either a fast Fourier transform (FFT) algorithm or a direct slow Fourier algorithm to compute the power spectrum.

Subsequently, for each month we chose the observation with the best statistics and we searched a more accurate estimate of T$_p$= $1/\nu_p$ as follows.

Let y_j be a folded and binned time series with N_b bins per each phase. If we fold y_j using several trial values of T$_p$, we can test the folded time series with a constant value $\bar{y}$ using the χ^2:

$$\chi^2 = \sum_{j=1}^{N_{dof}} \left(\frac{y_j - \bar{y}}{e_j} \right)^2 \tag{2.4}$$

where N_{dof}=N_b-1 is the number of degrees of freedom, while e_j is the error associated with y_j. If T$_p$ is wrong, $\chi^2 \simeq N_{dof}$, since the rotations do not sum up in phase; conversely, if T$_p$ is accurate, $\chi^2 \gg N_{dof}$, because the rotations sum up in phase and the folded profile deviates from the constant $\bar{y}$. Therefore, the best T$_p$ will be that which maximises eq.(2.4). To perform this analysis we used the `efsearch` software from Xronos (see Figure 2.5). The results are shown in Table 2.3.

Once we found the phase periods for each month, we chose to split all the time series in Table 2.2 but QEYE_20171118-024151_crab and QEYE_20171118-033311_crab using intervals of 30 s; for the

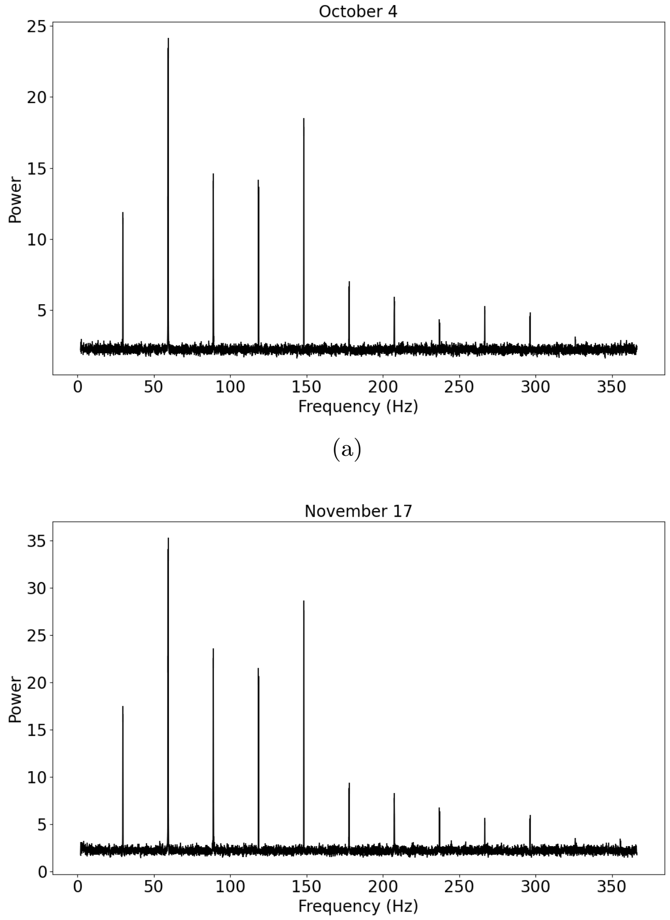

(a)

(b)

Figure 2.4: Figure (a): power spectrum of QEYE_20171004-040731_crab (October 4). Figure (b): power spectrum of QEYE_20171117-023605_crab (November 17). The binning time is set to 0.001 s for both the spectra.

observations performed on November 18 the poor counts rates required intervals of 60 s. Each interval was subsequently folded using the corresponding T$_p$ and 128 bins per phase to get the corresponding Crab pulse shape, namely the folded profile. In Figure 2.6 we show three representative folded profiles of October 4, November 17 and December 30.

2.3.2 Phase Fitting

A crucial step in pulsar timing analysis is the determination of the ToAs of the main pulse. As explained in section 1.2.2, in order to get the ToAs we need a suitable function to fit the Crab folded profiles. We used the sum of 16 Lorentzians provided by [4]:

$$f(x) = p \sum_{i=1}^{16} \frac{d_{i-1} b_i^2}{b_i^2 + (x - x_1 + h_{i-1})^2} + q \tag{2.5}$$

where p, q and x_1 are free parameters, while b_i, d_{i-1} and h_{i-1} are given in Table 2.4. The fractional phase of the main peak is given by x_1. In Figure 2.7 we show the fit performed over the Crab pulse shape of Figure 1.6(b) as an example of the accuracy provided by the function $f(x)$.

Calling $\phi^{'} = (t - t_0)/P_i$ the phase of a uniform rotator, where t_0 is the initial time, i.e. the reference epoch, and P_i the period at t_0, we can define the phase drift of the pulsar from a uniform rotator as:

$$\psi(t) = \phi(t) - \phi^{'}(t) \tag{2.6}$$

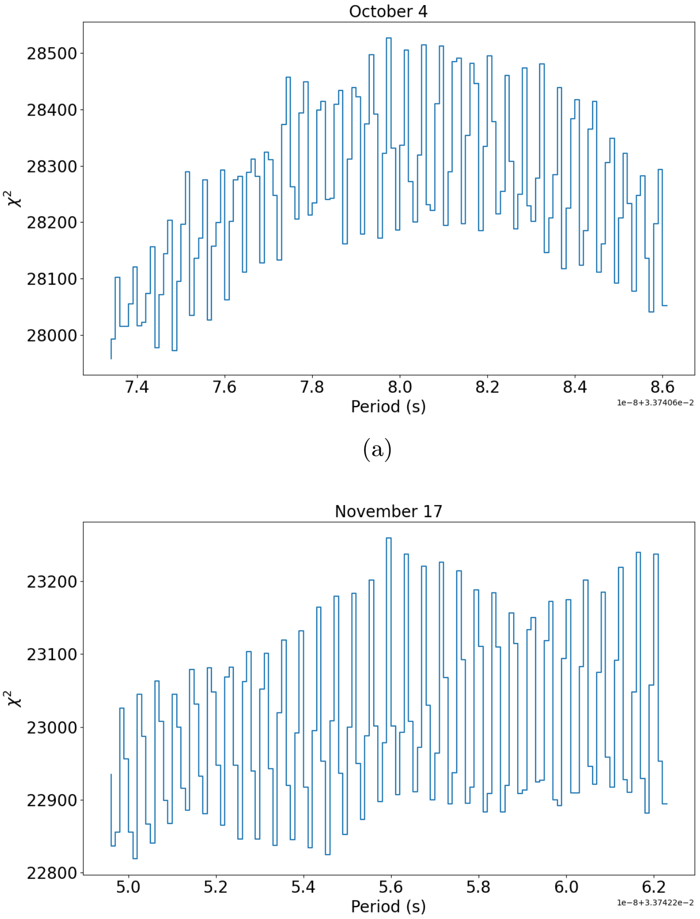

(a)

(b)

Figure 2.5: Figure (a): $\chi^2(\mathrm{T}_p)$ for QEYE_20171004-040731_crab (October 4). Figure (b): $\chi^2(\mathrm{T}_p)$ for QEYE_20171117-023605_crab (November 17). The figures were obtained with `efsearch` from Xronos [62].

where ϕ(t) is the actual Crab phase at time t. Through the Lorentzian fit of the folded profiles we can directly measure $\psi(t)$ = -x_1 ($\phi(t) < \phi^{'}(t)$ and $\psi(t) < 0$, if the pulsar is spinning down). We show the fractional phase drift of each observing night in Figure 2.8, where the uncertainties are given by the Lorentzian fit through the least squares method.

The next step is the cleaning of $-\psi$ to get rid of spurious data. We decided to remove the data which clearly did not follow the overall trend: on October 7 and on December 30 we removed the single points which deviated from the linear trend; on November 18 we removed all the data which were not consistent with the linear trend within a $\sim 3\sigma$ uncertainty.

Since the actual measurement of $\psi(t)$ returns only the fractional part, we need to add an integer to obtain a phase coherent timing evolution over the whole observing run. A clear example can be seen in Figure 2.8(b) where the drift covers a complete phase, i.e. -ψ $\sim$1, and then it starts again from zero: it is straightforward that we must add a phase to this turning point, which is the rotation the Crab lost with respect to the uniform rotator with reference period P_i. However, the integer phase jump cannot be directly recovered in this way when considering subsequent observing nights. We determined it for each observing run as follows.

For each run we plotted $-\psi$ as a function of time adding a certain number of integer phases and we fitted it with a parabola y:

$$y = ax^2 + bx + c \tag{2.7}$$

where a, b and c are free parameters and $x = t - t_0$ is the time since the reference epoch t_0. We chose t_0 as the mid time between the first and the last observations performed in a run.

Month	Phase Period T_p (s)	Reference Epoch (MJD)
October	0.0337406798	58031.6298229512487006
November	0.0337422560	58074.5857072874468015
December	0.0337438622	58118.0009388908640735

Table 2.3: Phase periods and reference epochs for each month.

Parameter	Value	Parameter	Value	Parameter	Value
b1	0.0146996	d0	1	h0	0
b2	0.0146996	d1	0.217538	h1	0.0295389
b3	0.0146996	d2	0.120438	h2	0.0452724
b4	0.0146996	d3	0.343795	h3	0.0159706
b5	0.0146996	d4	0.0274555	h4	-0.0405742
b6	0.00390605	d5	0.104503	h5	-0.004064
b7	0.0131649	d6	0.0524991	h6	-0.408426
b8	0.0517911	d7	0.0462601	h7	-0.493455
b9	0.0386609	d8	0.250336	h8	-0.400741
b10	0.0377745	d9	0.063293	h9	-0.445372
b11	0.0156592	d10	-0.0323015	h10	0.094 8912
b12	0.0325165	d11	-0.0176647	h11	0.133417
b13	0.0531056	d12	0.0128576	h12	0.355586
b14	0.209385	d13	0.00944315	h13	-0.0200141
b15	-0.0630249	d14	-0.00883256	h14	-0.261205
b16	0.0259154	d15	-0.00388652	h15	-0.153419

Table 2.4: Parameters of the function f(t) adopted to fit the Crab pulse profile, taken from [4].

Changing the number of integer rotations strongly affects the measured $-\psi$ and consequently the fit. If we add a defined number of rotations to the observed $-\psi$ values and we call this series $\widetilde{\phi}$, we can evaluate the χ^2:

$$\chi^2 = \sum_i^N \frac{\left(\widetilde{\phi}_i - y_i\right)^2}{(\sigma_i)^2} \tag{2.8}$$

where N is the number of data, y_i is the fit given by eq.(2.7) evaluated at the i-th point and σ_i is the error associated with $-\psi$, which is given by the Lorentzian fit through the least squares method. Since the $\widetilde{\phi}$ series differs only by an integer phase number, by minimizing the χ^2 we can find the best $\widetilde{\phi}$ series and consequently determine the exact number of rotations that occurred between two observing nights. Moreover, using the number of parameters N_{par} for a fit, namely three (a,b,c) in this case, we can define the number of degrees of freedom as $N_{dof} = N - N_{par}$ and compute the reduced χ^2 as:

$$\chi^2_{red} = \frac{\chi^2}{N_{dof}} \tag{2.9}$$

Once again, the minimum of eq.(2.9) shall give the exact number of rotations.

To quantify the reliability of the results obtained we calculated the p-value, which is defined as the probability of obtaining test results at least as probable as the results actually observed, assuming that the null hypothesis is correct. We chose the null hypothesis to be the membership of the data to the fitting curve. Therefore, if we choose a significance level of 5% and we get the p-value equal e.g. to 0.06, the fit is significant at p $\geq$ 5% and we cannot reject the null hypothesis at the 5% confidence level, i.e. we cannot say that data do not follow the fit. We must stress that we can never state that data do follow the fitting curve by means of the p-value: we are only allowed to reject or not reject the

Month	χ^2	χ^2_{red}	p-value	Number of Rotations
October	426.84	1.00	0.479425	12
November	213.31	1.29	0.006706	2
December	218.88	1.24	0.015488	0

Table 2.5: Best estimate for χ^2, χ^2_{red} and p-values for October, November and December. The corresponding number of rotations is indicated in the last column.

Month	ϕ_0	ν_0 (1/s)	$\dot{\nu_0}$ 10^{-10} (1/s^2)
October	-4.156 ± 0.002	29.63776505 ± 9×10^{-8}	-3.685 ± 0.002
November	-1.194 ± 0.004	29.63641011 ± 9×10^{-8}	-3.69 ± 0.04
December	-0.1782 ± 0.0003	29.6350207 ± 1×10^{-7}	-1.25 ± 1.04

Table 2.6: Timing solutions for October, November and December.

null hypothesis, but we are not allowed to accept it. Thus, according to our purposes, the p-value shall be large enough not to reject the null hypothesis.

We computed the χ^2, the χ^2_{red} and the p-values for different rotations, and we show the best results in Table 2.5. As it can be seen, we cannot reject the null hypothesis for October with a confidence level >5% and for December with a confidence level >1%. Concerning November, the p-value is smaller than 1%, but larger than 0.5%, which is still sufficiently high not to reject the null hypothesis with a confidence level larger than 3 Gaussian sigmas. The fitted phase drift for each month is shown in Figure 2.9, where we also added the number of rotations from Table 2.5 and the corresponding best fitting curve from eq.(2.7).

Finally, we computed the timing solution, i.e. ϕ_0, ν_0 and $\dot{\nu_0}$, for each month as follows. First, we estimated the coefficients a,b and c from the best fitting curve. Therefore we had:

$$ax^2 + bx + c = -\psi = \phi^{'}(x) - \phi(x) = \frac{x}{P_i} - \phi(x) \tag{2.10}$$

Furthermore, since we can rewrite $\phi(x)$ using a Taylor expansion as seen in eq.(1.29):

$$\begin{aligned}\phi(x) &= \phi_0 + \dot{\phi_0}x + \frac{1}{2}\ddot{\phi_0}x^2 && (2.11)\\ &= \phi_0 + \nu_0 x + \frac{1}{2}\dot{\nu_0}x^2 && (2.12)\end{aligned}$$

eq.(2.10) can be written as:

$$\begin{aligned}ax^2 + bx + c &= \frac{x}{P_i} - \phi_0 - \nu_0 x - \frac{1}{2}\dot{\nu_0}x^2 && (2.13)\\ ax^2 + bx + c &= -\phi_0 - \Big(\nu_0 - \frac{1}{P_i}\Big)x - \frac{1}{2}\dot{\nu_0}x^2 && (2.14)\end{aligned}$$

where all the terms with the subscript "0" are evaluated a $t = t_0$. We shall highlight that eq.(1.29) is computed up to the third order, while we truncated the equation at the second order: indeed, for a single observing run we cannot detect the contribution of the cubic term, since the timescale of the latter is considered to be roughly 180 days [4]. Therefore, we can limit ourselves to the quadratic term. By rearranging eq.(2.14) we derived the relations:

$$\begin{aligned}\phi_0 &= -c && (2.15)\\ \nu_0 &= -b + \frac{1}{P_i} && (2.16)\\ \dot{\nu_0} &= -2a && (2.17)\end{aligned}$$

which directly provide the timing solution. The results obtained for October, November and December are shown in Table 2.6. The associated errors were computed by means of the usual propagation of uncertainty formula:

$$\sigma_{\phi_0} = \sigma_c \tag{2.18}$$

$$\sigma_{\nu_0} = \sigma_b \tag{2.19}$$

$$\sigma_{\dot{\nu}_0} = 2\sigma_a \tag{2.20}$$

where σ_a, σ_b and σ_c are given by the least squares method of the fit in eq.(2.7).

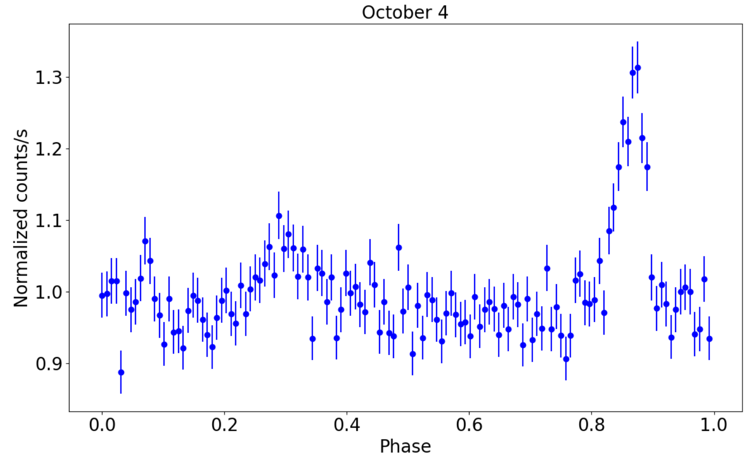

(a)

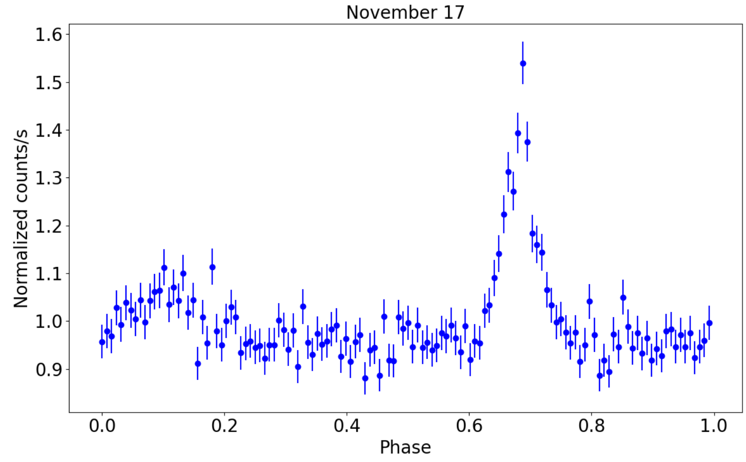

(b)

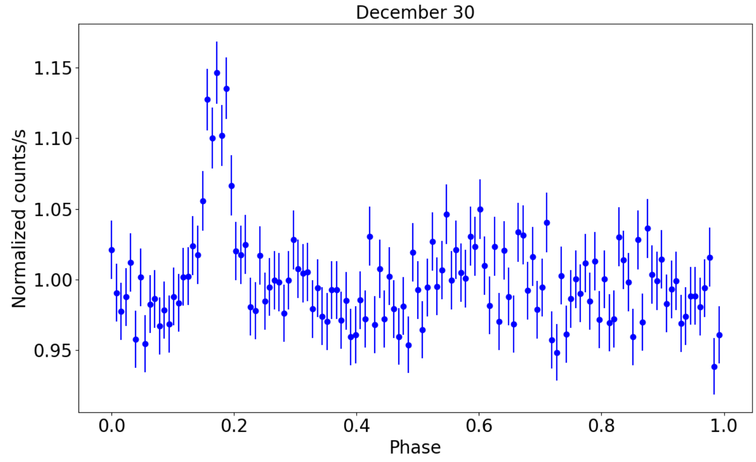

(c)

Figure 2.6: Folded profile of QEYE_20171004-040731_crab (Figure (a), October 4), QEYE_20171117-023605_crab (Figure (b), November 17) and QEYE_20171230-235440_crab (Figure (c), December 30). All the figures were obtained with `efold` from the Xronos software package [62] by folding an interval of 30 s and by using 120 bins per phase.

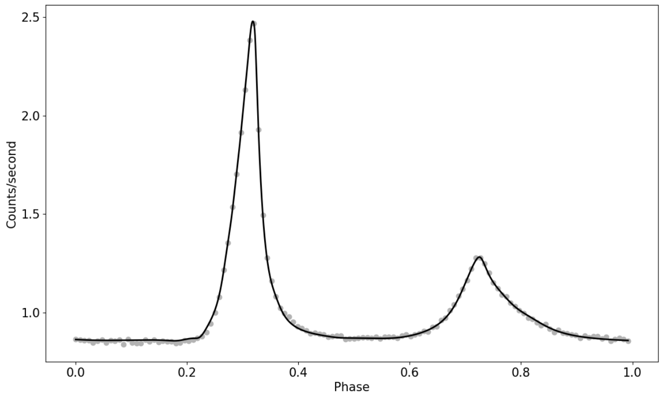

Figure 2.7: Fit of the Crab phase shape shown in Figure 1.6(b). Data are shown as grey dots, while the solid black line is the fit performed with eq.(2.5).

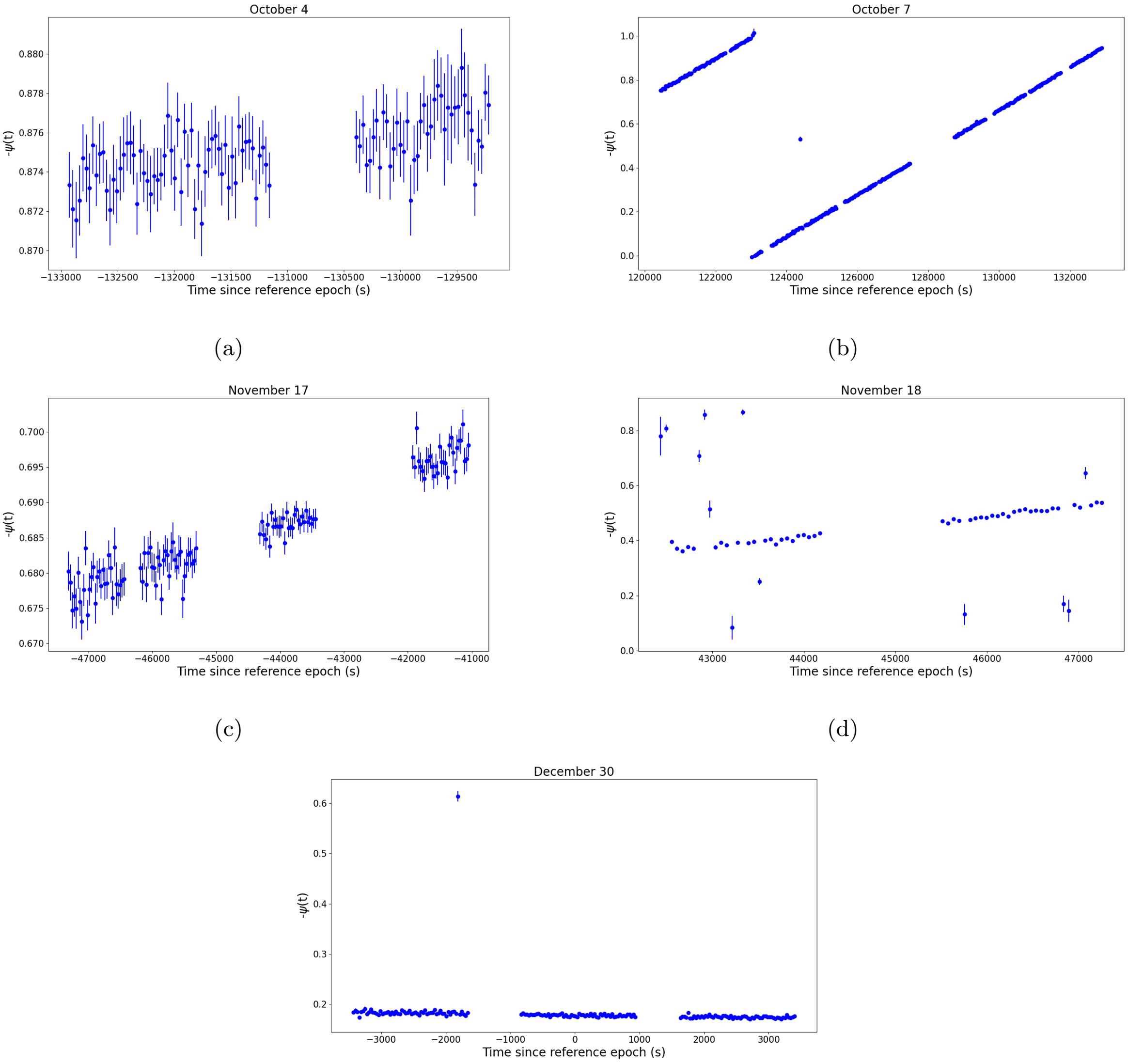

(a)

(b)

(c)

(d)

(e)

Figure 2.8: Phase drift -ψ(t) for October 4 (a), October 7 (b), November 17 (c), November 18 (d) and December 30 (e).

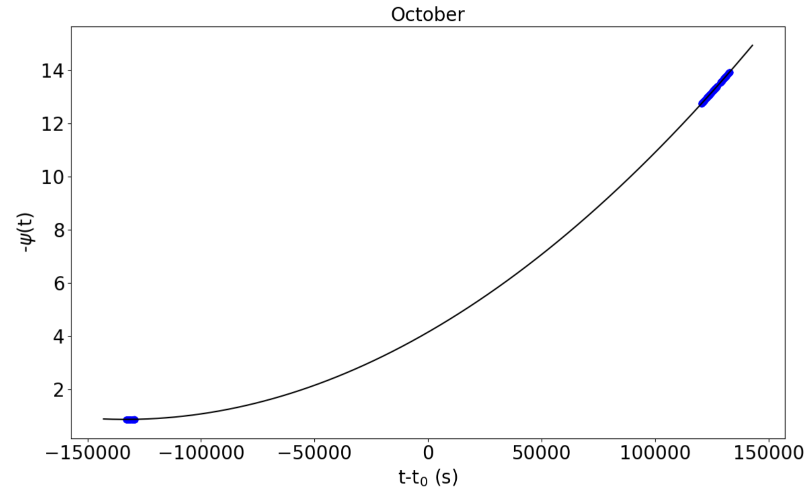

(a)

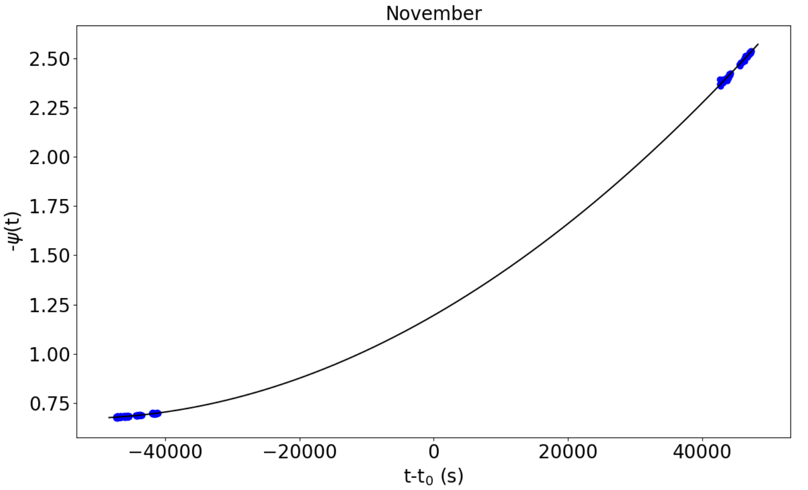

(b)

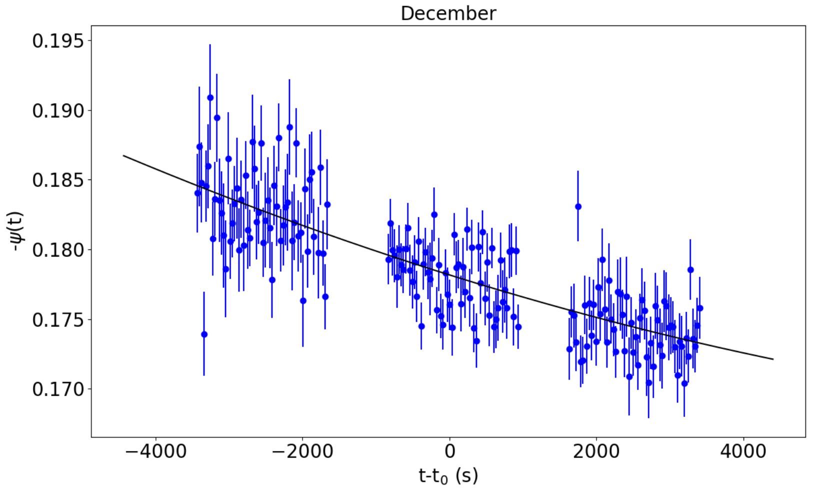

(c)

Figure 2.9: Fitted phase drift for (a) October, (b) November, (c) December. Data are shown as blue dots, while the fitting parabola is the solid black line.

Chapter 3

Results

3.1 Phase Coherent Optical Timing

To detect the glitch occurring on MJD 58064.555 we extrapolated the spin evolution measured with IFI+Iqueye during the observing runs of October and November towards the glitch epoch. Thus, by using the timing solutions shown in Table 2.6 we calculated the rotational frequency from:

$$\nu(t) = \nu_0 + \dot{\nu_0}(t - t_0) \tag{3.1}$$

From October 4 (MJD 58030.09130814821803) to November 8 (MJD 58064.555) we used the timing solution found for October; from November 8 (MJD 58064.555) to November 18 (MJD 58075.112496650025477) we used the timing solution found for November; from December 30 (MJD 58117.96120908628654) to December 31 (MJD 58118.04034257127205) we used the timing solution found for December. The rotational frequencies calculated in this way are shown in Figure 3.1 (upper panel). The error associated to eq.(3.1) is given by the usual propagation of uncertainty law:

$$\sigma_\nu = \sqrt{\sigma_{\nu_0}^2 + [(t - t_0)\sigma_{\dot{\nu_0}}]^2} \tag{3.2}$$

where σ_{ν_0} and $\sigma_{\dot{\nu_0}}$ are the uncertainties on ν_0 and $\dot{\nu_0}$ respectively. Plots as Figure 3.1 are usually called *butterfly plots.* To clearly show the detection of the glitch occurring on MJD 58064.555, we extrapolated the spin evolution in October ν_{oct} and subtracted it from the spin evolution of all epochs (Figure 3.1, lower panel).

Finally, we compared our results with those from the radio ephemeris of the Crab pulsar reported at the Jodrell Bank Centre for Astrophysics (hereafter JB) [9], [8]. We calculated the radio spin evolution by inserting the timing solutions provided by [8] (see [9] for further details) into eq.(3.1). The radio timing solutions and the time intervals chosen for this calculation are shown in Table 3.1. We shall highlight that time intervals were chosen in order to make the radio spin evolution ν(t) as smooth as possible. We also ignored the cubic term of the radio timing solutions, since is provides negligible contribution on the considered time span.

In Figure 3.1 we compare the butterfly plots for optical (dashed black line) and radio (solid grey line) observations. The uncertainties on the radio spin evolution are computed with eq.(3.2). The glitch epoch is indicated as a vertical dashed red line. Optical and radio data are clearly in agreement within 3σ uncertainty. Furthermore, we computed the optical frequency jump $\Delta\nu$ caused by the glitch and the ratio $\Delta\nu/\nu$, where ν is the pre-glitch frequency (Table 3.2): we found that $\Delta\nu/\nu = (0.44\pm0.11)\times10^{-6}$, which is consistent with the radio value $\Delta\nu/\nu = 0.516\times10^{-6}$ reported by [46].

Albeit the overall spin evolution inferred from the optical data is in agreement with that measured in the radio, it is important to stress that December data have a significant different slope. This deviation is probably due to the not enough accurate estimate of the spin derivative $\dot{\nu_0}$ for December, as seen in Table 2.6: only one observing night was available for this month, which turns out to be insufficient for an accurate measurement of $\dot{\nu_0}$. Hence we decided to exclude the results of December from the subsequent analysis.

Date	MJD	ν_0 (1/s)	$\dot{\nu}_0$ 10^{-15}(1/s^2)	Interval (MJD)
October 15	58041	29.6374670598 ± (2×10^{-10})	-368635.67 ± 0.22	58030.091 - 58064.555
November 4	58061	29.6368300767 ± (3×10^{-10})	-368616.01 ± 5.19	58058 - 58064.555
November 11	58068	29.6366215237 ± (72×10^{-10})	-369626.33 ± 106.30	58064.555 - 58068.7
November 22	58079	29.6362691342 ± (8×10^{-10})	-370857.08 ± 4.12	58068.7 - 58087.7
December 8	58095	29.6357567627 ± (7×10^{-10})	-370375.12 ± 5.53	58087.7 - 58102.2
December 24	58111	29.6352450494 ± (6×10^{-10})	-369986.53 ± 3.81	58102.2 - 58119

Table 3.1: Radio timing solutions provided by [8]. The time interval over which we calculated the spin evolution is also indicated in the last column.

ν Hz	$\Delta\nu$ μHz	$\Delta\nu/\nu$ 10^{-6}
29.6367167±0.0000007	13±3	0.44±0.11

Table 3.2: Crab rotational frequency ν before the glitch, frequency increase $\Delta\nu$ and relative frequency increase $\Delta\nu/\nu$ measured with IFI+Iqueye.

3.2 Phase Residuals

In Figure 3.2 we show the phase drift of the IFI+Iqueye observations and the corresponding parabola fits discussed in the previous chapter. To understand the post-glitch evolution of the pulsar, an important piece of information is given by the distribution of the residuals.

According to the pure photon counting noise, we expect it to be a gaussian [4]. However, any structured residual may indicate some phenomenon triggered by the glitch. Thus, we parsed the distributions using a binning of 15 μs for all observing nights except November 18, for which we needed a binning of ~100 μs due to low statistics. In Figure 3.3 we show the observed distributions fitted with a gaussian function centred at zero; the reduced χ^2 values and the dispersion σ (μs) are also shown in the figures. No significant evidence of structured residuals was found. We note that the values of the Gaussian σ are larger than those found by [4] because of the lower counting statistics of the data used in this thesis

3.3 Radio-Optical Delay

If we consider the light curve of the Crab pulsar throughout the electromagnetic spectrum, we can immediately see that the ToAs of the pulses are wavelength dependent: the main pulses are not aligned in time at different wavelengths [5]. This phase difference can be exploited to constrain the geometry of the emission region. Since the pulsation at a certain wavelength is due to a specific emission mechanism and is produced by charged particle with a given energy (which can be found only in certain regions of the magnetosphere), by comparing the main peak in different bands we can directly constrain the relative position of the emission regions.

In [5] the authors compared their optical observations, performed in October 2000 and November 2005, with the radio ephemeris provided by the JB [8]. The result showed that the optical pulse leads the radio one by 273 ± 65 μs, which they explained either as the angle between the orientations of the motion of the emitting particles ($\sim 3^o$) or with the optical radiation being produced ~ 90 km above the radio one in the magnetosphere. In a subsequent work [64] the estimate was improved to 255 ± 21 μs. Within this framework, a geometric distance of ~ 10 km roughly corresponds to an observed phase difference of ~ 0.001 [64].

A further effort was undertaken by [4]: using optical observations performed in 2009, the authors found that the optical pulse leads the radio one by ~ 240 μs in January and by ~ 160 μs in December. This result was interpreted as being induced by a misalignment between the optical and the radio

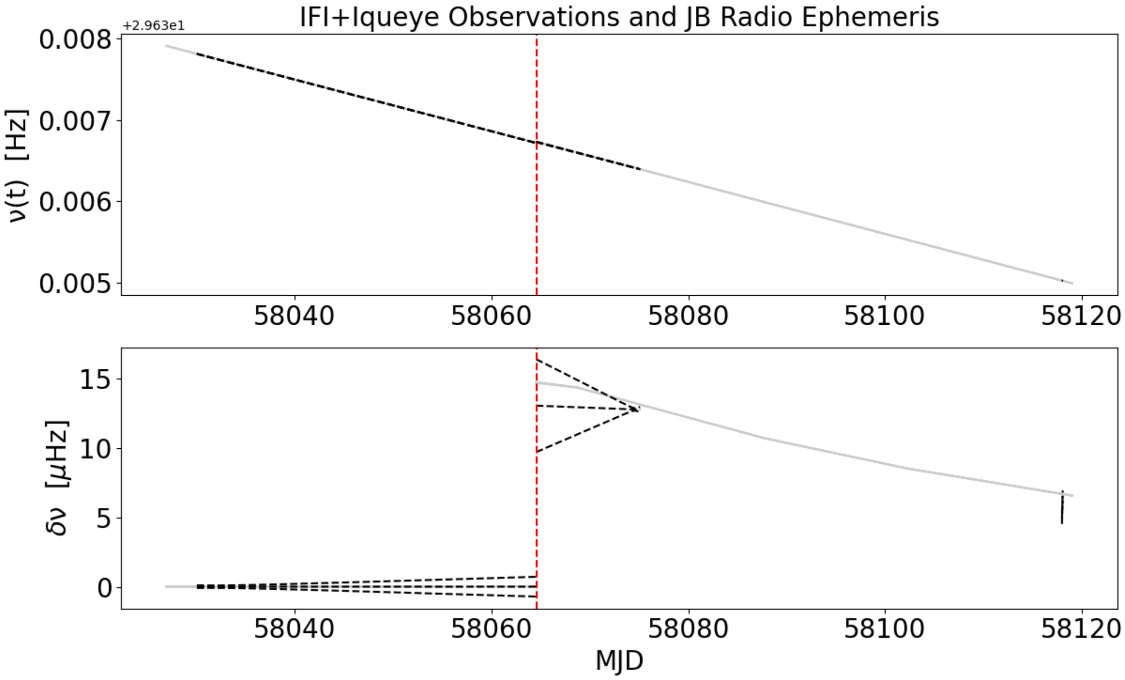

Figure 3.1: Upper panel: spin evolution between October and December. Optical (IFI+Iqueye) data are shown as dashed black lines, while radio (JB) observations from [8] are shown as solid grey lines. Lower Panel: spin evolution relative to the pre-glitch trend found in October. The glitch epoch MJD 58064.555 is indicated with a vertical dashed red line.

beams possibly caused by a slightly different orientation of the magnetic field. Moreover, they stressed that a different location of the emitting regions may not explain the observed time lag, because the electrons are highly relativistic and therefore any time delay due to the distinct paths travelled by the emitted photons and the electrons should be negligible.

Albeit the phase delay was considered constant hitherto, no reason suggests that this should be the case: by looking at the time evolution of the phase lag we can directly see whether geometrical rearrangements occur [7]. We have already anticipated in section 2.1 that a free precession of the spin axis is still debated; nevertheless, other spatial rearrangements such as magnetic field lines reconnections [32] or plasma density enhancements [45] could occur.

In this thesis we calculated the radio-optical time delay using the IFI+Iqueye optical data and the radio ephemeris provided by the JB [8]. From the timing solutions reported in Tables 2.6 and 3.1, we computed the corresponding optical $-\psi$ and radio $-\psi_{rad}$ phase drifts for October and November. The details of the calculation of the optical phase drift $-\psi$ are reported in section 2.3.2 (eq.(2.10)-(2.12)). The associated errors are given by the propagation of uncertainty formula:

$$\sigma_\psi = \sqrt{\sigma^2_{\phi_0} + [(t - t_{opt})\sigma_{\nu_0}]^2 + \left[\frac{1}{2}(t - t_{opt})^2\sigma_{\dot{\nu}_0}\right]^2} \tag{3.3}$$

where t_{opt} are the optical reference epochs found in Table 2.3 and the terms with the subscript "0" are evaluated at $t = t_{opt}$.

Concerning the radio phase drift, the timing solutions $\phi_{rad}(t_{rad})$, $\nu_{rad}(t_{rad})$ and $\dot{\nu}_{rad}(t_{rad})$ provided by the JB are referred to the reference epochs t_{rad} found in [8], which are different from the t_{opt} that we used for the optical analysis. Therefore, we evaluated the radio phase $\phi_{rad}(t_{opt})$ and the radio rotational frequency $\nu_{rad}(t_{opt})$ at the optical reference epochs t_{opt} by using the phase and the spin evolution laws:

$$\phi_{rad}(t_{opt}) = \phi_{rad}(t_{rad}) + \nu_{rad}(t_{rad})[t_{opt} - t_{rad}] + \frac{1}{2}\dot{\nu}_{rad}(t_{rad})[t_{opt} - t_{rad}]^2 \tag{3.4}$$

$$\nu_{rad}(t_{opt}) = \nu_{rad}(t_{rad}) + \dot{\nu}_{rad}(t_{rad})[t_{opt} - t_{rad}] \tag{3.5}$$

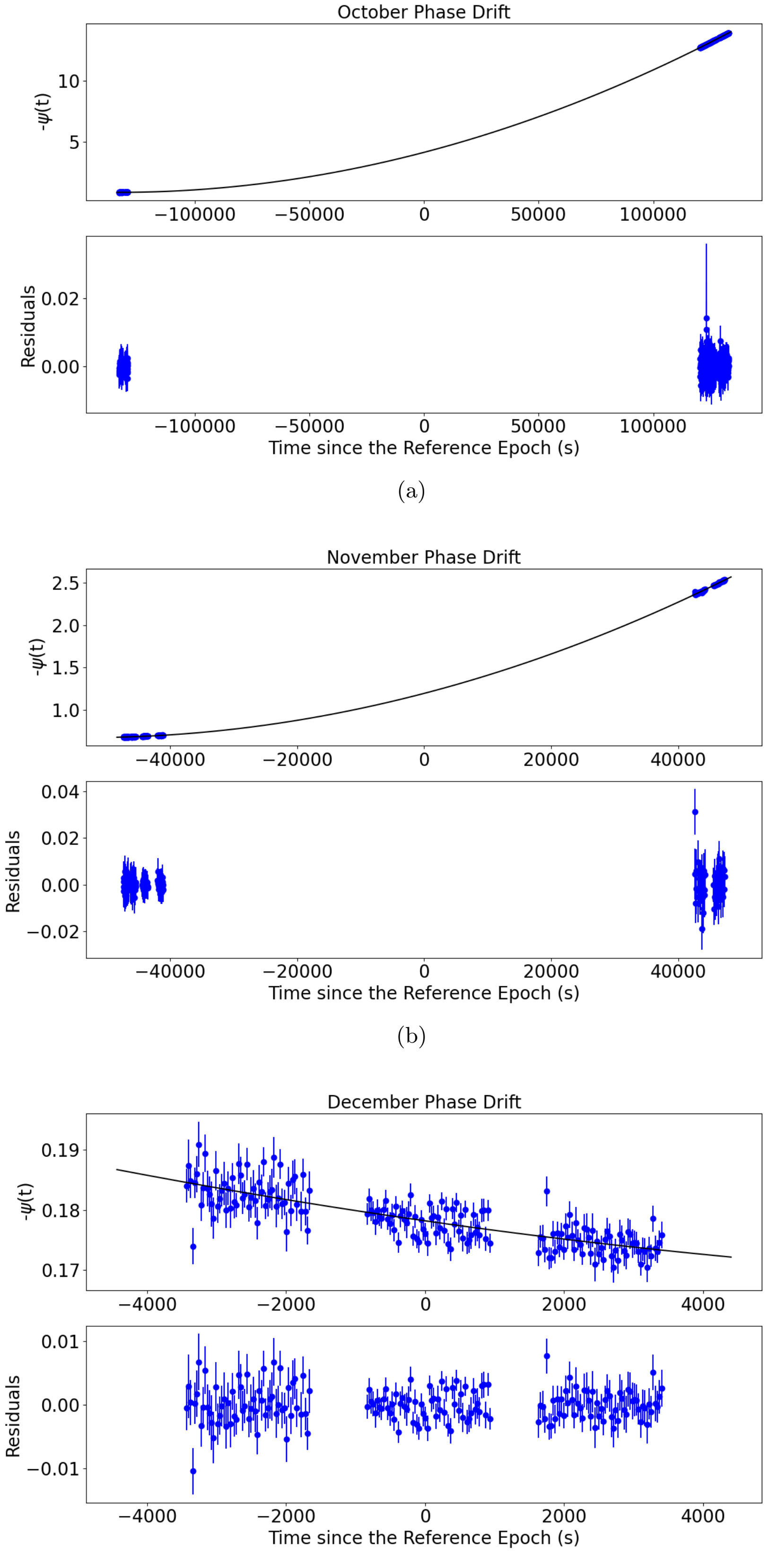

(a)

(b)

(c)

Figure 3.2: Fitted phase drift and residuals for (a) October, (b) November, (c) December IFI+Iqueye observations.

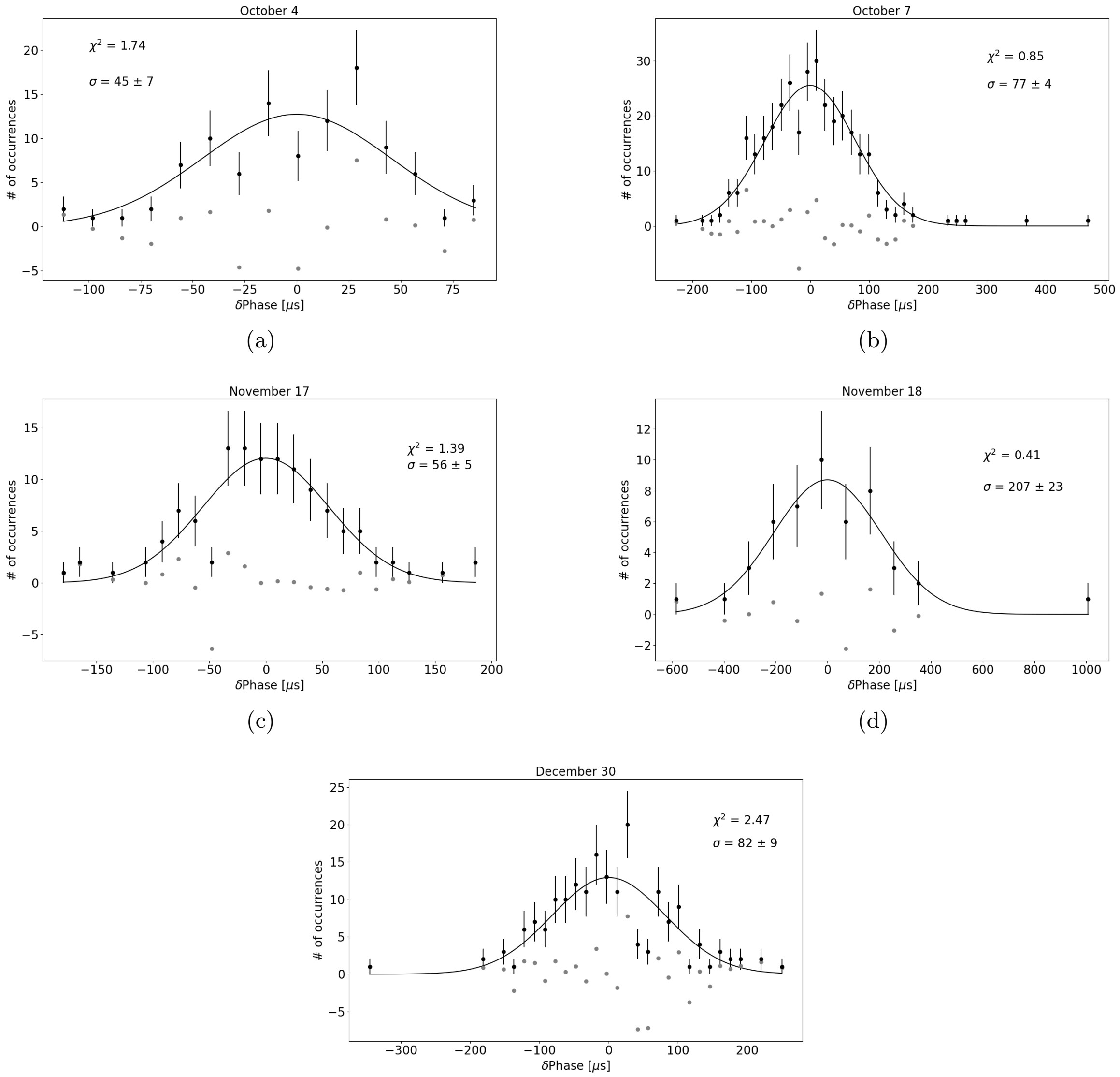

(a) (b) (c) (d) (e)

Figure 3.3: Phase residual distributions for the following IFI+Iqueye observing nights: (a) October 4, (b) October 7, (c) November 17, (d) November 18 and (e) December 30. The black dots represent the binned data; the solid black line is the gaussian fit and the grey dots are the differences between data and fitting curve. The reduced χ^2 values and the dispersion σ (μs) are shown.

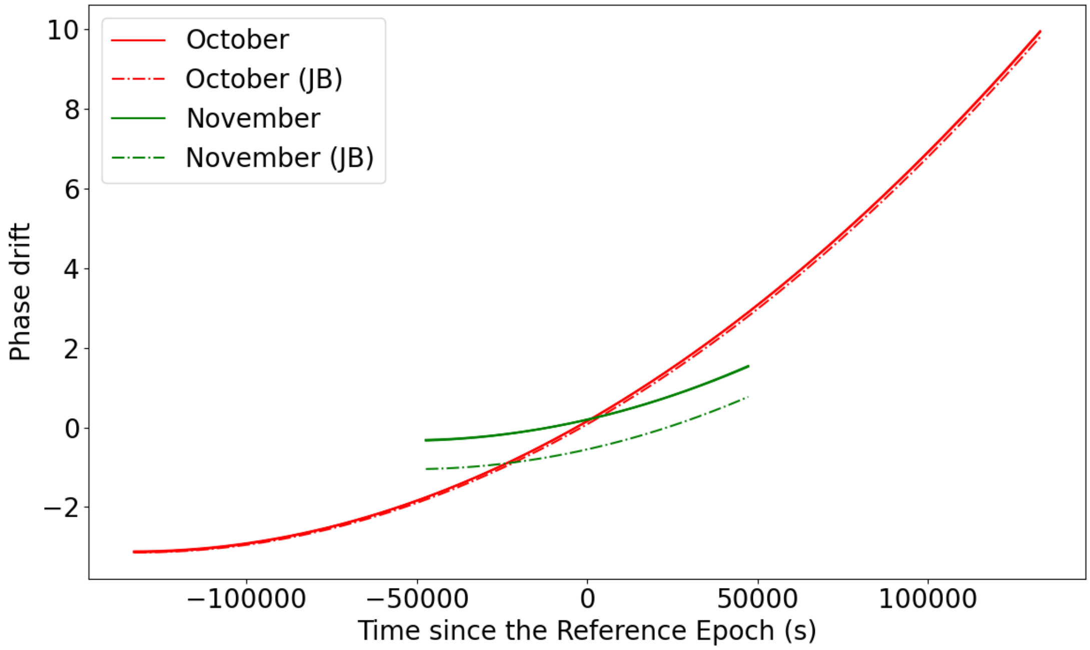

Figure 3.4: Radio (JB) and optical (IFI+Iqueye) phase drifts for October and November 2017.

where $\phi_{rad}(t_{rad}) = \mathrm{t}_{JPL}/(1/\nu_{rad}(t_{rad}))$ (see [8]).

We finally computed $-\psi_{rad}$ by means of eq.(2.10)-(2.12):

$$-\psi_{rad}(x) = -\phi_{rad}(t_{opt}) - \left[\nu_{rad}(t_{opt}) - \frac{1}{P_i}\right]x - \frac{1}{2}\dot{\nu}_{rad}(t_{opt})x^2 \tag{3.6}$$

where $x = t - t_{opt}$ and P_i are the periods from Table 2.3. The results are shown in Figure 3.4. The October butterfly plot from the optical observations (solid red line) is leading the radio solution (dashed red line), but the delay is much smaller than that computed in November. Indeed, the delay between the optical (solid green line) and the radio (dashed green line) increases dramatically after the glitch and the increment is clearly significantly larger than the error bars.

To quantify the delay we calculated $\psi - \psi_{rad}$, which is shown in Figure 3.5. At the reference epoch, the optical pulse is leading the radio one by 0.00262 ± 0.00007 s in October and by 0.0252 ± 0.0001 s in November. Thus, the delay increases after the glitch by an order of magnitude.

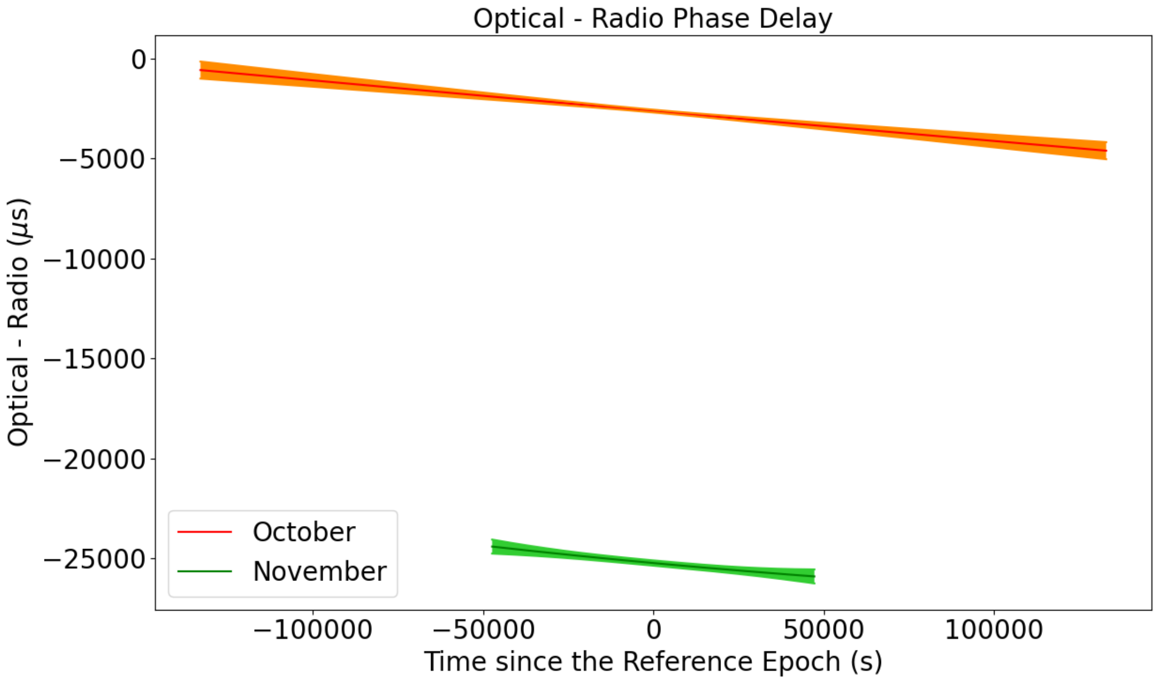

Figure 3.5: Delay between the IFI+Iqueye optical observations and the JB radio ephemeris, computed before and after the November 2017 glitch.

Chapter 4

Discussion and Conclusions

The Crab pulsar (PSR B0531+21; PSR J0534+2200) is one of the five isolated neutron stars which show a pulsating signal in both the optical and radio bands, together with the Vela (PSR B0833-45) pulsar, PSR B0540-69, PSR B0656+14, and Geminga (PSR B0630+17) [4]. Optical pulsations were recently observed also from the millisecond pulsar PSR J1023+0038 [65] and then independently confirmed by means of Aqueye+ mounted at the Copernicus Telescope in Asiago (Italy) [66]. The detection of pulsations in different bands allows a cross analysis throughout the electromagnetic spectrum, which can provide fundamental information on the geometry of the magnetospheric configuration.

In this thesis we parsed the observations of the Crab pulsar taken on 2017 October 4 and 7, November 17 and 18, December 30 with the very fast optical photon counter Iqueye [6], mounted at the 122 cm Galileo Telescope in Asiago (Italy) through a dedicated optical fiber interface (IFI). The time series provided by Iqueye was converted by means of the `TEMPO2` software package [59] to the SS barycentre.

We estimated the Crab rotational period in each observing runs through a power spectrum analysis of the time series. We subsequently split the time series into 30 s or 60 s intervals, according to the counting statistics of the observations, and we folded each interval with the corresponding period to get the so called folded profiles. Then the folded profile was fitted with an accurate fitting function [4] which directly provides the fractional ToAs of the main peak. After the cleaning of spurious data, following [4] we determined the number of rotations needed to reconstruct the timing solution using a χ^2 procedure. Thanks to this analysis we were able to build an optical phase coherent timing solution for the Crab pulsar in each observing run (Table 2.6). The timing residual distributions obtained are well described by a Gaussian, in agreement with what expected for pure photon counting noise [4].

It is well known from radio data [46] that on MJD 58064.555 a glitch occurred; to pinpoint this spin up event in the optical domain we compared the spin evolution inferred from our timing solutions with the JB radio ones [8]. We found that optical and radio data clearly agree within the 3σ uncertainties and we estimated the optical frequency jump $\Delta\nu = 13 \pm 3$ μHz caused by the glitch and the ratio $\Delta\nu/\nu = (0.44 \pm 0.11) \times 10^{-6}$, which are both consistent with the radio values $\Delta\nu = 15$ μHz and $\Delta\nu/\nu = 0.516 \times 10^{-6}$ reported by [46], respectively. This result further confirms that glitches are wavelength-independent phenomena. Moreover, this is the first glitch detected with Iqueye.

The pulsation at a certain wavelength is produced through a given emission mechanism by particles in a given energy range, which can occur only in certain regions of the magnetosphere. Hence by looking at the wavelength-dependent phase drift we can directly constrain the geometry of the emission regions and the magnetosphere which surrounds the pulsar.

This effort has already been undertaken by many authors throughout the electromagnetic spectrum. The time delay between radio pulses on the one hand and X-rays and γ-rays ones on the other have been measured (see, for example, [67] and [68]) and the latter are clearly leading the former. Concerning the radio and the optical, the comparison between optical and radio phase drift led to a time lag of 273 ± 65 μs in [5], with the optical pulse leading the radio one. [5] suggested that this phase lag could be explained either as the angle between the orientations of the motion of the emitting particles, namely a misalignment between the radio and the optical beamed emissions of $\sim 3^o$, or with the optical radiation being produced $\sim$ 90 km above the radio one in the magnetosphere. The same authors further improved their estimate to 255 ± 21 μs in a subsequent work [64]. In a more recent paper [4] the authors estimated a phase delay of $\sim$ 240 μs for 2009 January and $\sim$ 160 μs for 2009 December. They also highlighted that a different location of the emitting regions is an unlikely explanation because the electrons are highly relativistic and therefore any time delay due to the distinct paths travelled by the emitted photons and the electrons should be negligible. Thus the most plausible model is a misalignment between the radio and the optical beams of 1.5^o - 3^o [4].

Within this framework, we compared our optical phase drift with that provided by the JB ephemeris. We found that the optical pulse is leading the radio one, in agreement with the aforementioned works, but the estimated time lag is $\sim$ 0.00262 ± 0.00007 s in October. Although the pulsar frequency noise may affect our estimate (optical and radio measurements are not simultaneous), the difference appears significant. More importantly, after the MJD 58064.555 glitch the time lag jumped up to 0.0252 ± 0.0001 s, corresponding to $\sim$ 0.5 in phase. Such a change in the time delay has never been observed before. This lag can be interpreted as a major rearrangement of the geometry of the magnetosphere triggered by the glitch. If confirmed, this would be a direct evidence of a spatial reconfiguration of the magnetosphere and a clear evidence of the time delay variability.

This interpretation is further supported by the decrease in the Crab soft X-rays (3.0-4.5 keV) polarization after a glitch occurred on 2019 July 23 [69]. Previous evidence of rearrangements of the magnetosphere induced by the glitch were also suggested to explain some very low probability events which occurred around the 2016 December 12 glitch of the Vela pulsar [57]: a broad pulse, followed by a null one, both preceding two pulses with lower linear polarization; an increase in the mean and a reduction in the variance of the timing residuals, during which Vela exhibited the glitch. Furthermore, within a 2.6 s interval the radio pulses arrived later than expected, in agreement with our results.

A feasible process which could explain this phenomenon is an abrupt change in the orientations between the optical and the radio beams, which may be caused by the variation of the angle between the spin and the magnetic axes triggered by the glitch. Even if any free precession of the spin axis would be damped by the internal superfluid [51] and [52], its motion with respect to the magnetic axis of the pulsar was already invoked to explain the observed 35-day cycle in the Hercules X-1 pulsating binary [70] and, more recently, the observed variation of the braking index of the Crab pulsar [31].

Moreover, the free precession has been invoked to model the long term cyclical variations of the spin by many authors: evolution of the pulse shape and the slow down of PSR B1828-11 were described by harmonically sinusoids with periodicity $\sim$ 1000, 500 and 250 days by [54]; variations with periodicity of $\sim$ 1250 days in PSR B1642-03 were modelled by [53]; the Crab pulsar, the Vela pulsar (PSR B0833-45), PSR B1642-03, PSR B1828-11, the remnant of SN 1987A and Hercules X-1 were all tested for free precession of the rotation axis by [55], who suggested that the motion of the spin axis may be caused by glitches. Furthermore, since the energy loss due to the braking mechanisms depends on the angle between the rotation and the magnetic axes, this inclination angle should tend to a value which minimizes the energy loss as the neutron star ages. The estimated value which the inclination angle should tend to is $\pi/2$ [56].

In light of these considerations, future works should try to test whether a glitch could directly affect the spin axis (by inducing a free precession) and/or the geometry of the magnetosphere by means of broader observations and by parsing more of these events. We will therefore be able to constrain the emission region and the physical conditions within the magnetosphere [64]. On the other hand, a theoretical effort is needed to explain the fundamental reason which allows the free precession to survive despite the superfluid damping and to unambiguously model this mechanism in order to constrain physical quantities like the moment of inertia. Moreover, by parsing glitches due to different triggering mechanisms we can further investigate how dissimilar glitches affect the magnetosphere. Finally, the variability of the time lag between optical and radio pulse could also be taken into account to possibly explain the inconsistencies found in the literature [5]: different estimates for the delay could be in agreement if the time lag is not constant over time, i.e. if the magnetosphere is ceaselessly changing.

References

[1] T. Gold. “Rotating Neutron Stars as the Origin of the Pulsating Radio Sources”. In: *Nature* 218.5143 (May 1968), pp. 731–732. DOI: `10.1038/218731a0`.

[2] P. Ghosh. *Rotation and Accretion Powered Pulsars*. World Scientific Series in Astronomy and Astrophysics Vol.10. World Scientific Publishing Co. Pte. Ltd., 2007.

[3] A. G. Lyne et al. “45 years of rotation of the Crab pulsar”. In: *Monthly Notices of the Royal Astronomical Society* 446.1 (Jan. 2015), pp. 857–864. DOI: `10.1093/mnras/stu2118`. arXiv: `1410.0886 [astro-ph.HE]`.

[4] L. Zampieri et al. “Optical phase coherent timing of the Crab nebula pulsar with Iqueye at the ESO New Technology Telescope”. In: *Monthly Notices of the Royal Astronomical Society* 439.3 (Apr. 2014), pp. 2813–2821. DOI: `10.1093/mnras/stu136`. arXiv: `1402.2571 [astro-ph.HE]`.

[5] T. Oosterbroek et al. “Absolute timing of the Crab Pulsar at optical wavelengths with superconducting tunneling junctions”. In: *Astronomy and Astrophysics* 456.1 (Sept. 2006), pp. 283–286. DOI: `10.1051/0004-6361:20065254`.

[6] G. Naletto et al. “Iqueye, a single photon-counting photometer applied to the ESO new technology telescope”. In: *Astronomy and Astrophysics* 508.1 (Dec. 2009), pp. 531–539. DOI: `10.1051/0004-6361/200912862`.

[7] L. Zampieri et al. “(Very) Fast astronomical photometry for meter-class telescopes”. In: *Contributions of the Astronomical Observatory Skalnate Pleso* 49.2 (May 2019), pp. 85–96. arXiv: `1908.03396 [astro-ph.IM]`.

[8] Jodrell Bank Centre for Astrophysics. URL: `http://www.jb.man.ac.uk/~pulsar/crab.html`.

[9] A. G. Lyne, R. S. Pritchard, and F. Graham Smith. “23 years of Crab pulsar rotational history.” In: *Monthly Notices of the Royal Astronomical Society* 265 (Dec. 1993), pp. 1003–1012. DOI: `10.1093/mnras/265.4.1003`.

[10] M. S. Longair. *High Energy Astrophysics*. Cambridge University Press, 2011.

[11] R. N. Manchester et al. “The Australia Telescope National Facility Pulsar Catalogue”. In: *Astronomical Journal* 129.4 (Apr. 2005), pp. 1993–2006. DOI: `10.1086/428488`. arXiv: `astro-ph/0412641 [astro-ph]`.

[12] M. Kramer et al. “Tests of General Relativity from Timing the Double Pulsar”. In: *Science* 314.5796 (Oct. 2006), pp. 97–102. DOI: `10.1126/science.1132305`. arXiv: `astro-ph/0609417 [astro-ph]`.

[13] M. A. Alpar et al. “Giant glitches and pinned vorticity in the VELA and other pulsars.” In: *Astrophysical Journal, Letters* 249 (Oct. 1981), pp. L29–L33. DOI: `10.1086/183652`.

[14] W. Baade and F. Zwicky. “Cosmic rays from super-novae”. In: *Proceedings of the National Academy of Sciences* 20.5 (1934), pp. 259–263.

[15] R. Giacconi et al. “Evidence for x Rays From Sources Outside the Solar System”. In: *Physical Review Letter* 9.11 (Dec. 1962), pp. 439–443. DOI: `10.1103/PhysRevLett.9.439`.

[16] A. Hewish et al. “Observation of a Rapidly Pulsating Radio Source”. In: *Nature* 217.5130 (Feb. 1968), pp. 709–713. DOI: `10.1038/217709a0`.

[17] Anna L. Watts et al. "Dense matter with eXTP". In: *Science China Physics, Mechanics, and Astronomy* 62.2, 29503 (Feb. 2019), p. 29503. DOI: `10.1007/s11433-017-9188-4`. arXiv: `1812.04021 [astro-ph.HE]`.

[18] Feryal Özel and Paulo Freire. "Masses, Radii, and the Equation of State of Neutron Stars". In: *Annual Review of Astronomy and Astrophysics* 54 (Sept. 2016), pp. 401–440. DOI: `10.1146/annurev-astro-081915-023322`. arXiv: `1603.02698 [astro-ph.HE]`.

[19] J. Pétri. "Theory of pulsar magnetosphere and wind". In: *Journal of Plasma Physics* 82.5, 635820502 (Oct. 2016), p. 635820502. DOI: `10.1017/S0022377816000763`. arXiv: `1608.04895 [astro-ph.HE]`.

[20] F. Pacini. "Energy Emission from a Neutron Star". In: *Nature* 216.5115 (Nov. 1967), pp. 567–568. DOI: `10.1038/216567a0`.

[21] A. R. Choudhuri et al. *The physics of fluids and plasmas: an introduction for astrophysicists*. Cambridge University Press, 1998.

[22] Peter Goldreich and William H. Julian. "Pulsar Electrodynamics". In: *Astrophysical Journal* 157 (Aug. 1969), p. 869. DOI: `10.1086/150119`.

[23] D. Melrose. "Pulse Emission Mechanisms". In: *Young Neutron Stars and Their Environments*. Ed. by Fernando Camilo and Bryan M. Gaensler. Vol. 218. IAU Symposium. Jan. 2004, p. 349. arXiv: `astro-ph/0308471 [astro-ph]`.

[24] Bryan M. Gaensler and Patrick O. Slane. "The Evolution and Structure of Pulsar Wind Nebulae". In: *Annual Review of Astronomy and Astrophysics* 44.1 (Sept. 2006), pp. 17–47. DOI: `10.1146/annurev.astro.44.051905.092528`. arXiv: `astro-ph/0601081 [astro-ph]`.

[25] M. Kramer et al. "A Periodically Active Pulsar Giving Insight into Magnetospheric Physics". In: *Science* 312.5773 (Apr. 2006), pp. 549–551. DOI: `10.1126/science.1124060`. arXiv: `astro-ph/0604605 [astro-ph]`.

[26] L. A. Fowler, G. A. E. Wright, and D. Morris. "Unusual properties of the pulsar PSR 1822-09." In: *Astronomy and Astrophysics* 93 (Jan. 1981), pp. 54–61.

[27] G. Petit and P. Tavella. "Pulsars and time scales." In: *Astronomy and Astrophysics* 308 (Apr. 1996), pp. 290–298.

[28] A. G. Lyne. "Mode changing in pulsar radiation". In: *Monthly Notices of the Royal Astronomical Society* 153 (Jan. 1971), 27P. DOI: `10.1093/mnras/153.1.27P`.

[29] D. Morris et al. "Changes in the average pulse shape of PSR 0355+54 at 11 CM wavelength." In: *Astronomy and Astrophysics* 84 (Apr. 1980), pp. 260–262.

[30] D. R. Lorimer and M. Kramer. *Handbook of Pulsar Astronomy*. Vol. 4. 2004.

[31] A. Lyne et al. "Evolution of the Magnetic Field Structure of the Crab Pulsar". In: *Science* 342.6158 (Nov. 2013), pp. 598–601. DOI: `10.1126/science.1243254`. arXiv: `1311.0408 [astro-ph.HE]`.

[32] A. Čadež et al. "What brakes the Crab pulsar?" In: *Astronomy and Astrophysics* 587, A99 (Mar. 2016), A99. DOI: `10.1051/0004-6361/201526490`. arXiv: `1512.05606 [astro-ph.HE]`.

[33] Jingbo Wang et al. "Recent glitches detected in the Crab pulsar". In: *Astrophysics and Space Science* 340.2 (Aug. 2012), pp. 307–315. DOI: `10.1007/s10509-012-1058-x`. arXiv: `1203.4291 [astro-ph.HE]`.

[34] Werner Becker, Mike G. Bernhardt, and Axel Jessner. "Autonomous Spacecraft Navigation With Pulsars". In: *Acta Futura* 7 (Nov. 2013), pp. 11–28. arXiv: `1305.4842 [astro-ph.HE]`.

[35] G. Hobbs, A. G. Lyne, and M. Kramer. "An analysis of the timing irregularities for 366 pulsars". In: *Monthly Notices of the Royal Astronomical Society* 402.2 (Feb. 2010), pp. 1027–1048. DOI: `10.1111/j.1365-2966.2009.15938.x`. arXiv: `0912.4537 [astro-ph.GA]`.

[36] J. J. Hester. "The Crab Nebula : an astrophysical chimera." In: *Annual Review of Astronomy and Astrophysics* 46 (Sept. 2008), pp. 127–155. DOI: `10.1146/annurev.astro.45.051806.110608`.

[37] K. Lundmark. “Suspected New Stars Recorded in Old Chronicles and Among Recent Meridian Observations”. In: *Publications of the ASP* 33.195 (Oct. 1921), p. 225. DOI: `10.1086/123101`.

[38] E. P. Hubble. “Novae or Temporary Stars”. In: *Leaflet of the Astronomical Society of the Pacific* 1.14 (Jan. 1928), p. 55.

[39] J. J. L. Duyvendak. “Further Data Bearing on the Identification of the Crab Nebula with the Supernova of 1054 A.D. Part I. The Ancient Oriental Chronicles”. In: *Publications of the ASP* 54.318 (Apr. 1942), pp. 91–94. DOI: `10.1086/125409`.

[40] N. U. Mayall and J. H. Oort. “Further Data Bearing on the Identification of the Crab Nebula with the Supernova of 1054 A.D. Part II. The Astronomical Aspects”. In: *Publications of the ASP* 54.318 (Apr. 1942), pp. 95–104. DOI: `10.1086/125410`.

[41] David H. Staelin and III Reifenstein Edward C. “Pulsating Radio Sources near the Crab Nebula”. In: *Science* 162.3861 (Dec. 1968), pp. 1481–1483. DOI: `10.1126/science.162.3861.1481`.

[42] J. M. Comella et al. “Crab Nebula Pulsar NP 0532”. In: *Nature* 221.5179 (Feb. 1969), pp. 453–454. DOI: `10.1038/221453a0`.

[43] W. J. Cocke, M. J. Disney, and D. J. Taylor. “Discovery of Optical Signals from Pulsar NP 0532”. In: *Nature* 221.5180 (Feb. 1969), pp. 525–527. DOI: `10.1038/221525a0`.

[44] R. Bühler and R. Blandford. “The surprising Crab pulsar and its nebula: a review”. In: *Reports on Progress in Physics* 77.6, 066901 (June 2014), p. 066901. DOI: `10.1088/0034-4885/77/6/066901`. arXiv: `1309.7046 [astro-ph.HE]`.

[45] A. Shearer et al. “Enhanced Optical Emission During Crab Giant Radio Pulses”. In: *Science* 301.5632 (July 2003), pp. 493–495. DOI: `10.1126/science.1084919`. arXiv: `astro-ph/0308271 [astro-ph]`.

[46] B. Shaw et al. “The largest glitch observed in the Crab pulsar”. In: *Monthly Notices of the Royal Astronomical Society* 478.3 (Aug. 2018), pp. 3832–3840. DOI: `10.1093/mnras/sty1294`. arXiv: `1805.05110 [astro-ph.HE]`.

[47] C. M. Espinoza et al. “Neutron star glitches have a substantial minimum size”. In: *Monthly Notices of the Royal Astronomical Society* 440.3 (May 2014), pp. 2755–2762. DOI: `10.1093/mnras/stu395`. arXiv: `1402.7219 [astro-ph.HE]`.

[48] Brynmor Haskell and Andrew Melatos. “Models of pulsar glitches”. In: *International Journal of Modern Physics D* 24.3, 1530008 (Jan. 2015), p. 1530008. DOI: `10.1142/S0218271815300086`. arXiv: `1502.07062`.

[49] C. M. Espinoza et al. “A study of 315 glitches in the rotation of 102 pulsars”. In: *Monthly Notices of the Royal Astronomical Society* 414.2 (June 2011), pp. 1679–1704. DOI: `10.1111/j.1365-2966.2011.18503.x`. arXiv: `1102.1743 [astro-ph.HE]`.

[50] M. Yu et al. “Detection of 107 glitches in 36 southern pulsars”. In: *Monthly Notices of the Royal Astronomical Society* 429.1 (Feb. 2013), pp. 688–724. DOI: `10.1093/mnras/sts366`. arXiv: `1211.2035 [astro-ph.HE]`.

[51] J. Shaham. “Free precession of neutron stars: role of possible vortex pinning.” In: *Astrophysical Journal* 214 (May 1977), pp. 251–260. DOI: `10.1086/155249`.

[52] Armen Sedrakian, Ira Wasserman, and James M. Cordes. “Precession of Isolated Neutron Stars. I. Effects of Imperfect Pinning”. In: *Astrophysical Journal* 524.1 (Oct. 1999), pp. 341–360. DOI: `10.1086/307777`. arXiv: `astro-ph/9801188 [astro-ph]`.

[53] T. V. Shabanova, A. G. Lyne, and J. O. Urama. “Evidence for Free Precession in the Pulsar B1642-03”. In: *Astrophysical Journal* 552.1 (May 2001), pp. 321–325. DOI: `10.1086/320438`. arXiv: `astro-ph/0101282 [astro-ph]`.

[54] I. H. Stairs, A. G. Lyne, and S. L. Shemar. “Evidence for free precession in a pulsar”. In: *Nature* 406.6795 (Aug. 2000), pp. 484–486. DOI: `10.1038/35020010`.

[55] D. I. Jones and N. Andersson. "Freely precessing neutron stars: model and observations". In: *Monthly Notices of the Royal Astronomical Society* 324.4 (July 2001), pp. 811–824. DOI: `10.1046/j.1365-8711.2001.04251.x`. arXiv: `astro-ph/0011063 [astro-ph]`.

[56] V. S. Beskin and E. E. Nokhrina. "On the role of the current loss in radio pulsar evolution". In: *Astrophysics and Space Science* 308.1-4 (Apr. 2007), pp. 569–573. DOI: `10.1007/s10509-007-9307-0`. arXiv: `astro-ph/0608689 [astro-ph]`.

[57] Jim Palfreyman et al. "Alteration of the magnetosphere of the Vela pulsar during a glitch". In: *Nature* 556.7700 (Apr. 2018), pp. 219–222. DOI: `10.1038/s41586-018-0001-x`.

[58] Luca Zampieri et al. "Intensity interferometry with Aqueye+ and Iqueye in Asiago". In: *Proceedings of the SPIE*. Vol. 9907. Society of Photo-Optical Instrumentation Engineers (SPIE) Conference Series. Aug. 2016, 99070N. DOI: `10.1117/12.2233688`. arXiv: `1609.01134 [astro-ph.IM]`.

[59] G. B. Hobbs, R. T. Edwards, and R. N. Manchester. "TEMPO2, a new pulsar-timing package - I. An overview". In: *Monthly Notices of the Royal Astronomical Society* 369.2 (June 2006), pp. 655–672. DOI: `10.1111/j.1365-2966.2006.10302.x`. arXiv: `astro-ph/0603381 [astro-ph]`.

[60] R. T. Edwards, G. B. Hobbs, and R. N. Manchester. "TEMPO2, a new pulsar timing package - II. The timing model and precision estimates". In: *Monthly Notices of the Royal Astronomical Society* 372.4 (Nov. 2006), pp. 1549–1574. DOI: `10.1111/j.1365-2966.2006.10870.x`. arXiv: `astro-ph/0607664 [astro-ph]`.

[61] I. S. Shklovskii. "Possible Causes of the Secular Increase in Pulsar Periods." In: *Soviet Astronomy* 13 (Feb. 1970), p. 562.

[62] Nasa High Energy Astrophysics Science Archive Research Center (Heasarc). *HEAsoft: Unified Release of FTOOLS and XANADU*. Aug. 2014. ascl: `1408.004`.

[63] Nasa High Energy Astrophysics Science Archive Research Center (Heasarc). URL: `http://heasarc.gsfc.nasa.gov/ftools`.

[64] T. Oosterbroek et al. "Simultaneous absolute timing of the Crab pulsar at radio and optical wavelengths". In: *Astronomy and Astrophysics* 488.1 (Sept. 2008), pp. 271–277. DOI: `10.1051/0004-6361:200809751`. arXiv: `0806.3634 [astro-ph]`.

[65] F. Ambrosino et al. "Optical pulsations from a transitional millisecond pulsar". In: *Nature Astronomy* 1 (Oct. 2017), pp. 854–858. DOI: `10.1038/s41550-017-0266-2`. arXiv: `1709.01946 [astro-ph.HE]`.

[66] Luca Zampieri et al. "Precise optical timing of PSR J1023+0038, the first millisecond pulsar detected with Aqueye+ in Asiago". In: *Monthly Notices of the RAS* 485.1 (May 2019), pp. L109–L113. DOI: `10.1093/mnrasl/slz043`. arXiv: `1903.08930 [astro-ph.HE]`.

[67] L. Kuiper et al. "Absolute timing with IBIS, SPI and JEM-X aboard INTEGRAL. Crab main-pulse arrival times in radio, X-rays and high-energy gamma -rays". In: *Astronomy and Astrophysics* 411 (Nov. 2003), pp. L31–L36. DOI: `10.1051/0004-6361:20031353`. arXiv: `astro-ph/0309178 [astro-ph]`.

[68] Arnold H. Rots, Keith Jahoda, and Andrew G. Lyne. "Absolute Timing of the Crab Pulsar with the Rossi X-Ray Timing Explorer". In: *Astrophysical Journal, Letters* 605.2 (Apr. 2004), pp. L129–L132. DOI: `10.1086/420842`. arXiv: `astro-ph/0403187 [astro-ph]`.

[69] Hua Feng et al. "Re-detection and a possible time variation of soft X-ray polarization from the Crab". In: *Nature Astronomy* 4 (May 2020), pp. 511–516. DOI: `10.1038/s41550-020-1088-1`.

[70] K. A. Postnov, M. E. Prokhorov, and N. I. Shakura. "On the Observational Appearances of a Freely Precessing Neutron Star in Hercules X-1". In: *High-Energy Astrophysics. American and Soviet Perspectives*. Jan. 1991, p. 307.

Appendices

We show the Python script used to fit the folded profile and to determine the position of the main peak x_1 (see section 2.3.2). Moreover, this module displays the phase drift as a function of the detection time (Time since the reference epoch) and eventually creates a csv file with the x_1 values for the whole observing run. The example presented here is for December data.

```
import numpy as np
import matplotlib.pyplot as plt
import scipy as sp
from scipy.optimize import curve_fit
from astropy.io import fits
from astropy.table import Table
import csv

class date:
    def __init__(self,mjd,epoch,step):
        self.mjd = mjd
        self.epoch = epoch
        self.step = step

PATH20 = ’.../QEYE_20171230-235440_fold_30s_test.fef’
PATH21 = ’.../QEYE_20171231-003758_fold_30s_test.fef’
PATH22 = ’.../QEYE_20171231-011907_fold_30s_test.fef’

path_list = [PATH20, PATH21, PATH22]

### start day and time of each observation session ###
t20 = date(58117.961209086285322,58118.0009388908640735,30)
t21 = date(58117.991281496316642,58118.0009388908640735,30)
t22 = date(58118.019856460156944,58118.0009388908640735,30)
t = [t20, t21, t22]

### values for the Lorentzians ###
b = np.array([0.0146996, 0.0146996, 0.0146996, 0.0146996, 0.0146996,
0.00390605, 0.0131649, 0.0517911, 0.0386609, 0.0377745, 0.0156592,
0.0325165, 0.0531056, 0.209385, -0.0630249, 0.0259154])
d = np.array([1, 0.217538, 0.120438, 0.343795, 0.0274555, 0.104503,
0.0524991, 0.0462601, 0.250336,0.063293, -0.0323015, -0.0176647,
0.0128576, 0.00944315, -0.00883256, -0.00388652])
h = np.array([0,0.0295389, 0.0452724, 0.0159706, -0.0405742, -0.004064,
-0.408426, -0.493455, -0.400741, -0.445372, 0.0948912, 0.133417,
0.355586, -0.0200141, -0.261205, -0.153419])

### sum of 16 Lorentzians ###
def lorentz(x,p,q,x1):
    lorentz_list = []
    for i in range(len(x)):
        lorentz_list.append(p*np.sum((d*b**2)/(b**2+(x[i]-x1+h)**2))+q)
    return np.array(lorentz_list)

def sec_converter(time_array,epoch):
    time1 = time_array - epoch
    time = time1/(1./86400)
```

```
    return time

### fit of the main peak ###
def main():
    hdul = []
    x1_val_list = []
    x1_err_list = []
    mjd_list = []
    for j in range(len(path_list)):
        hdul.append(fits.open('{}'.format(path_list[j])))
        x1_val = []
        x1_err = []
        mjd = t[j].mjd
        epoch = t[j].epoch
        step = t[j].step
        for i in range(1,len(hdul[j])):
            events = Table.read(hdul[j],hdu=i)
            x = events['PHASE']
            y = events['RATE1']
            ylist = list(y)
            x1_guess = x[ylist.index(max(ylist))]
            p_guess = max(ylist)
            q_guess = np.min(y)
            pguess = [p_guess,q_guess,x1_guess]
            popt, pcov = curve_fit(lorentz, x, y, p0 = pguess)
            p,q,x1 = popt[0],popt[1],popt[2]
            errors = np.sqrt(np.diag(pcov))
            x1_err.append(errors[2])
            x1_val.append(x1)
            mjd_list.append(mjd+(i-1)*step*(1./86400))
        x1_val_list += x1_val
        x1_err_list += x1_err
    x1_val_array = np.array(x1_val_list)
    x1_err_array = np.array(x1_err_list)
    time_array = np.array(mjd_list)

### plot with seconds ###
    plt.errorbar(sec_converter(time_array, t20.epoch), x1_val_array,
    yerr = x1_err_array, fmt='ob')
    plt.xticks(fontsize=20)
    plt.yticks(fontsize=20)
    plt.xlabel('Time since reference epoch (s)',size=20)
    plt.ylabel('-$\psi$(t)', size=20)
    plt.title('December',size=20)
    plt.show()

### to create a csv file with all the data ###
    time_sec = sec_converter(time_array,t1.epoch)
    f=open('December_data.csv','w+')
    f.write('#Data for December 30 \n')
    f.write('#seconds are referred to the epoch \n')
    f.write('#MJD \t -PSI \t PSI_ERR \t SECONDS \n')
    for l in range():
        riga='%5.14f  %5.14f  %.14f  %6.8f\n' % (time_array[l],
        x1_val_array[l], x1_err_array[l], time_sec[l])
        f.write(riga)
    f.close()

if __name__=='__main__':
    main()
```

The following Python script was used to fit the phase drift and to return the timing solution. It takes the csv files generated through the previous module and returns either the timing solution or the plot of the fitted phase drift and the residuals (Figure 3.2). We show an example for December.

```
import numpy as np
import matplotlib.pyplot as plt
import scipy as sp
from scipy.optimize import curve_fit

month_data = 'December_data.csv'
p1 = 0.0337438622

def parabola(x,a,b,c):
    p = []
    for i in range(len(x)):
        p.append(a*x[i]**2+b*x[i]+c)
    return np.array(p)

### data analysis ###
def func(l):
    data = np.genfromtxt('{}'.format(month_data))
    mjd = data[:,0]
    phase = data[:,1]
    phase_err = data[:,2]
    sec = data[:,3]

    popt, pcov = curve_fit(parabola, sec, phase)
    a,b,c = popt[0],popt[1],popt[2]
    errors = np.sqrt(np.diag(pcov))

    nu_dot = -2*a
    err_nudot = 2*errors[0]
    nu = -b+1./p1
    err_nu = errors[1]
    phi = -c
    err_phi = errors[2]
    chisq = np.sum(((phase-(a*sec**2+b*sec+c))**2)/((phase_err)**2))
    ndof = len(phase)-3.
    chisq_red = chisq/ndof
    if l==1:
        return phi, err_phi, nu, err_nu, nu_dot, err_nudot,
        chisq, chisq_red
    elif l==2:
        return sec, phase, phase_err, a, errors[0], b, errors[1],
        c, errors[2]

### return some values of the fitted data ###
def values():
    phi,err_phi,nu,err_nu,nu_dot,err_nudot,chisq,chisq_red = func(1)
    print('phi:',phi,'+-',err_phi, '\n')
    print('nu:',nu, '+-', err_nu, '\n')
    print('nu_dot:',nu_dot, '+-', err_nudot, '\n')
    print('chisq:',chisq, '\n')
    print('chisq_red:',chisq_red, '\n')

### phase drift plot fitted and time residuals ###
def grafico():
    sec, phase, phase_err,a,err_a,b,err_b,c,err_c = func(2)

    ax1 = plt.subplot(211)
    ax1.errorbar(sec,phase, yerr=phase_err, fmt='ob')
    sec2 = np.arange(np.min(sec)-1000, np.max(sec)+1000)
    ax1.errorbar(sec2, a*sec2**2+b*sec2+c, fmt='-k')
    ax1.set_ylabel('-$\psi$(t)',size=20)
    ax1.tick_params(axis='both', labelsize=20)
```

```
    ax1.set_title('December', size=20)

    ax2 = plt.subplot(212, sharex=ax1)
    residuals = phase - (a*sec**2+b*sec+c)
    err_res = phase_err + np.sqrt((err_a*sec**2)**2+(err_b*sec)**2)
    ax2.errorbar(sec, residuals,yerr=err_res, fmt='ob')
    ax2.set_xlabel('Time since the Reference Epoch (s)',size=20)
    ax2.set_ylabel('Residuals', size=20)
    ax2.tick_params(axis='both', labelsize=20)
    plt.show()

if __name__ == '__main__':
    grafico()
```